

University of Alberta

# Photoluminescence Study of Nd Enriched Si-Nanocluster Glass

by

A. Nicole MacDonald



A thesis submitted to the Faculty of Graduate Studies and Research in partial  
fulfillment of the requirements for the degree of Master of Science

Department of Physics

Edmonton, Alberta  
Spring 2007



Library and  
Archives Canada

Bibliothèque et  
Archives Canada

Published Heritage  
Branch

Direction du  
Patrimoine de l'édition

395 Wellington Street  
Ottawa ON K1A 0N4  
Canada

395, rue Wellington  
Ottawa ON K1A 0N4  
Canada

*Your file* *Votre référence*  
*ISBN: 978-0-494-29991-3*  
*Our file* *Notre référence*  
*ISBN: 978-0-494-29991-3*

#### NOTICE:

The author has granted a non-exclusive license allowing Library and Archives Canada to reproduce, publish, archive, preserve, conserve, communicate to the public by telecommunication or on the Internet, loan, distribute and sell theses worldwide, for commercial or non-commercial purposes, in microform, paper, electronic and/or any other formats.

The author retains copyright ownership and moral rights in this thesis. Neither the thesis nor substantial extracts from it may be printed or otherwise reproduced without the author's permission.

#### AVIS:

L'auteur a accordé une licence non exclusive permettant à la Bibliothèque et Archives Canada de reproduire, publier, archiver, sauvegarder, conserver, transmettre au public par télécommunication ou par l'Internet, prêter, distribuer et vendre des thèses partout dans le monde, à des fins commerciales ou autres, sur support microforme, papier, électronique et/ou autres formats.

L'auteur conserve la propriété du droit d'auteur et des droits moraux qui protègent cette thèse. Ni la thèse ni des extraits substantiels de celle-ci ne doivent être imprimés ou autrement reproduits sans son autorisation.

---

In compliance with the Canadian Privacy Act some supporting forms may have been removed from this thesis.

Conformément à la loi canadienne sur la protection de la vie privée, quelques formulaires secondaires ont été enlevés de cette thèse.

While these forms may be included in the document page count, their removal does not represent any loss of content from the thesis.

Bien que ces formulaires aient inclus dans la pagination, il n'y aura aucun contenu manquant.

  
**Canada**

*To*  
*Blanche MacDonald*

## Abstract

Silicon nanocrystals can act as “sensitizers” for the luminescence of rare earth ions. Our group has shown that *amorphous* silicon clusters demonstrate a similarly effective energy transfer mechanism with respect to the rare earths, and have several other attractive properties as well. In this work, the interactions between amorphous silicon nanoclusters and Nd ions were investigated. Silicon nanocluster specimens doped with different concentrations of neodymium were characterized by continuous wave and pulsed photoluminescence measurements as a function of specimen temperature and pumping power. A model for the system is developed and compared to the data in an attempt to describe the nanocluster-Nd interaction. The results presented here show that amorphous silicon nanoclusters are effective sensitizers for the main Nd optical transitions, and offer advantages associated with a lower temperature fabrication. Several limitations were also found which must be overcome if these materials are to be used in light emitting devices.

## Acknowledgements

I've had the pleasure of meeting many people during my time at the University of Alberta, all of whom have enriched my experience here in one way or another. I am extremely grateful to my Master's supervisor, Dr. Al Meldrum, for all of his support and advice. His enthusiasm, patience, guidance, and understanding have made this a fun and exciting experience. It was an honour to learn in his lab. I am very thankful to Cindy Blois, who trained or helped train me on every piece of equipment I've used outside of the laser lab, also for introducing to me the novelty of margarita pitchers. I want to thank Aaron Hryciw, who I thoroughly enjoyed working both in the lab and on the blackboard. Thanks to all the current and former members of the Meldrum lab, especially to Megan Glover, Florian Lenz, and Sulan Kuai. It has been a privilege collaborating with Ray DeCorby and Dr. Quan Li as well as members of their groups. I'd like to thank the great technical staff, especially Don Mullin for his genius solutions to so many problems in 101 and for re-introducing me to tequila and Guinness. Many thanks to Greg Popowich, for teaching me to be calm in the face of the TEM. Also Ken Marsh, Tony Walford, Yolande Peske, Steve Rogers, Jay Haverstock, Jim MacKinnon and the machine shop gurus. Many thanks to the administrative staff in the office, especially Sarah Derr. I have had the opportunity to learn from amazing teachers here at the university, in particular, I want to thank Dr. Andrzej Czarnecki and Dr. Massimo Boninsegni for their insightful lectures on statistical and quantum mechanics. Thank you to all the great friends I've made here, especially Brad Schultz for the hours of wicked entertainment, Angela Beltaos for the hours of heart to hearts, and Aaron and Emily Slepko for the hours of gourmet meals. I'd like to thank my grandmother, Blanche MacDonald, for being a role model, who, at 86, still chops her own firewood and checks out handsome fellows. Finally, I'd like to thank the people who cheered me on and supported me over the years - my parents Catherine and Richard; my sisters Vanessa, Julia, and Stephanie; and Michael Steinitz, who is an honorary MacDonald. And, finally, my thanks to David Cooke. His love and support was more than I could ever ask for.

# Table of Contents

<b>1</b>	<b>Motivation</b>	<b>1</b>
<b>2</b>	<b>Background</b>	<b>6</b>
2.1	Nd electronic configuration and transitions . . . . .	6
2.2	Er in Silicon . . . . .	8
2.3	Er in Si-nanocrystal systems . . . . .	10
2.4	Er in amorphous Si-nanocluster systems . . . . .	13
2.5	Mechanisms of non-radiative recombination . . . . .	15
<b>3</b>	<b>Specimen Synthesis</b>	<b>20</b>
3.1	Set A . . . . .	21
3.2	Set B . . . . .	21
3.3	Graduated concentration sample . . . . .	21
3.4	Nd doped SiO <sub>2</sub> and Nd doped Silica laser glass . . . . .	23
3.5	Film processing . . . . .	23
<b>4</b>	<b>Experimental</b>	<b>24</b>
4.1	Electron Microprobe Analysis . . . . .	24
4.2	Optical studies . . . . .	25
4.2.1	Absorption and transmission . . . . .	26
4.2.2	Wavelength-resolved PL . . . . .	27
4.2.3	Time resolved PL measurements . . . . .	28
4.2.4	Low temperature measurements . . . . .	29
<b>5</b>	<b>Results</b>	<b>32</b>
5.1	Film composition . . . . .	32
5.2	Si nanocluster PL . . . . .	33
5.3	Absorption measurements . . . . .	36
5.4	Nd PL of specimens annealed from 300 to 1100 °C . . . . .	38
5.5	Nd PL of the graduated-Nd-concentration sample . . . . .	43
5.6	Nd PL for various pump energies and powers . . . . .	50

TABLE OF CONTENTS

5.7	Nd PL at low temperature . . . . .	52
5.8	Nd PL from Nd-doped SiO <sub>2</sub> thin film . . . . .	56
5.9	Nd PL from Nd-doped silica laser glass . . . . .	56
<b>6</b>	<b>Discussion</b>	<b>60</b>
6.1	Comparison of nanocluster PL in doped and undoped specimens . . . . .	60
6.2	Estimate of Nd environment based on PL . . . . .	61
6.3	Effect of annealing temperature on Nd PL . . . . .	62
6.4	Effect of Nd concentration on Nd PL . . . . .	63
6.5	Nd-to-nanocluster transfer processes . . . . .	64
6.6	Functional form of Nd radiative decay . . . . .	65
6.7	Nd excitation cross-section . . . . .	65
6.8	Model . . . . .	67
<b>7</b>	<b>Conclusion</b>	<b>73</b>
	<b>Bibliography</b>	<b>75</b>
<b>A</b>	<b>Exciton energy levels</b>	<b>82</b>
<b>B</b>	<b>Quantum confinement</b>	<b>83</b>
<b>C</b>	<b>Accousto-optic modulator</b>	<b>85</b>
<b>D</b>	<b>Photomultiplier tube</b>	<b>86</b>

# List of Tables

2.1	1.06 $\mu\text{m}$ peak of Nd photoluminescence in various host glasses. $\sigma$ is the cross-section, $\tau_{1.06}$ is the lifetime of the Nd ${}^4F_{3/2} \rightarrow {}^4I_{11/2}$ transition centred at 1060 nm, and $\tau_{all}$ is the total radiative decay time of the system (measured over all transitions). Modified after [1].	9
4.1	Spectrometers used in wavelength resolved photoluminescence measurements. . . . .	26
4.2	Laser lines of the HeCd and Ar-ion lasers. . . . .	31
4.3	Filters used in wavelength- and time-resolved photoluminescence measurements. . . . .	31
5.1	Electron microprobe results of 5 different samples (atomic %). Results are averaged over five points per sample. . . . .	33
5.2	Comparison of the integrated Si nanocluster PL from the undoped [22] and doped (sample set A) SiO films, normalized to the 400°C anneal. . . . .	35
5.3	$\tau$ and $\beta$ from fits to linearized data over various concentrations. . .	46
5.4	Nd PL time constants ( $\tau$ ) for rise and decay, $\beta$ , and goodness of fit ( $R^2$ is the coefficient of determination of a linear regression). . . . .	55
5.5	Peak wavelengths and heights from Gaussian fits. . . . .	58
6.1	Effective excitation cross-sections for low concentrations of Nd in SiO.	67



# List of Figures

1.1	The lower 4f-shell energy levels of an Er ion. . . . .	2
1.2	The variation of attenuation in silica optical fibers with wavelength. The three principal windows of operation are indicated and ‘OH <sup>-</sup> ’ symbols indicate increased attenuation due to the presence of hydroxyl radicals in the cable material. Adapted after [2]. . . . .	4
2.1	Energy levels of Nd <sup>3+</sup> . . . . .	7
2.2	Model of Er doped crystalline Si. Phonon-assisted Si excitation creates an electron-hole pair which subsequently excites an Er ion through Auger process. . . . .	10
2.3	Non-radiative processes in Er-doped Si nanocrystals: a) Auger processes from nanocrystal to rare earth and from rare earth to nanocrystal, b) Migration and defect quenching. . . . .	11
2.4	Model of Er Förster excitation of Er by an excited crystalline Si nanocrystal. . . . .	12
2.5	Model of Er Auger excitation Er doped SiO <sub>2</sub> containing crystalline Si nanoclusters. . . . .	12
2.6	Mechanisms of non-radiative recombination in the RE-doped silicon nanocluster glass include A) back transfer (left), or impurity auger excitation (right), B) second excitation of an ion into a higher excited state, C) excitation diffusion, and D) co-operative up-conversion. . . . .	18
2.7	Sketch of excitation diffusion. Black arrows are energy transfers, white circles are Si nanoclusters, black circles are Nd ions, grey circles are Nd ions coupled to quenching sites. . . . .	19
3.1	Nd deposition set up of graduated concentration sample. Curves are density contour lines of vapour emission. The SiO source was much further away such that the density of vapour emission is considered constant over the film. . . . .	22
4.1	Absorption and transmission setup. . . . .	26
4.2	Wavelength resolved PL setup. . . . .	27

## LIST OF FIGURES

4.3	PL of a low Nd concentration sample with interference filters. PL bands recorded during time-resolved PL measurements are shown by the blue (Nd) and red (Si-nc) lines, along with the PL spectra recorded with only the 550 nm BPF in black. . . . .	28
4.4	Time resolved pump signal rise and fall (488 nm line of the Ar laser) as recorded by a Si diode. Taken by fellow grad student, A. Hryciw. . . . .	29
4.5	Time resolved measurement setup with AOM. . . . .	30
4.6	Low temperature time resolved setup. . . . .	31
5.1	PL from specimen set A (0.14 atomic % Nd) (black) and an undoped SiO film (grey), both annealed at 400°C. A) PL spectra from samples used in lifetime measurements. Oscillations in the 600 to 700 nm range are due interference effects of the thin films. (B) Time resolved data for the broad Si nanocluster band. . . . .	34
5.2	Absorption spectra of various concentrations of Nd across the graduated-Nd-concentration sample. The detector limit is 350 nm, according to Ocean Optics specifications. . . . .	37
5.3	Photoluminescence data for Specimen Set A (0.14 atomic % Nd) for various annealing temperatures. The Nd PL at ~900 nm decreases with increasing annealing temperatures. . . . .	38
5.4	Photoluminescence data from a doped (0.14 atomic % Nd) SiO film annealed at 300°C (grey circles) and the fit (black line) to the sum of multiple Gaussian curves (red lines). . . . .	39
5.5	A) Nd PL data from set A, with the Gaussian fit to the nanocluster PL subtracted from the data. B) Integrated luminescence intensity of the Nd PL (set A), and the undoped SiO Si nanocluster PL (undoped SiO plot modified after [3]) . . . . .	40
5.6	Photoluminescence data for Specimen Set B (0.44 atomic % Nd) annealed at 300, 400 and 500°C. Data from two spectrometers are stitched together at approximately 950 nm to display a greater spectral range. . . . .	42
5.7	A) PL taken at intervals across the graduated sample. B) PL intensity from the Si nanoclusters and Nd ions, integrated from 550 to 800 nm and from 860 to 1000 nm, respectively. . . . .	43
5.8	Time resolved Nd PL from the graduated Nd concentration sample. A) rise data, B) decay data. . . . .	44
5.9	Time resolved Nd PL from the graduated Nd concentration sample. A) rise, B) decay. . . . .	47
5.10	Time resolved Nd PL (normalized) of the graduated-Nd-concentration sample. A) rise, B) decay. . . . .	48
5.11	$\tau$ from fits to linearized data over various concentrations . . . . .	49

LIST OF FIGURES

5.12	$\beta$ from fits to linearized data over various concentrations . . . . .	49
5.13	Nd PL (0.44 atomic % Nd). Inset shows the integrated PL intensity as a function of excitation energy. . . . .	50
5.14	Integrated Nd PL intensity as a function of pump power at 476 nm (0.44 atomic % Nd). . . . .	51
5.15	PL temperature dependence of the 0.2 atomic % Nd sample. Inset shows integrated PL intensities of Si and Nd PL as a function temperatures. . . . .	52
5.16	Temperature dependence of the Nd PL sub-peaks, fit by Gaussians. A) peak centre, B) peak intensity. . . . .	53
5.17	Time resolved Nd PL ( $\sim 0.2$ atomic % Nd) at 4, 77, 293 K. A) rise, B) decay. . . . .	54
5.18	Nd PL data and Gaussian fits to A) Nd in the nanocluster films (denoted as Nd in a-Si nc), and B) Nd in silica laser glass. . . . .	57
5.19	Nd PL spectra from doped silica laser glass (black line) and Nd doped (0.44 atomic % Nd) amorphous Si nanocluster glass (grey circles). The stitch line indicates where data from two spectrometers were joined. . . . .	58
5.20	Time resolved Nd PL of the Nd laser glass. Lines are fits to the data. . . . .	59
6.1	Nd PL from SiO doped with 0.44 atomic % Nd (Nd:SiO). Plots of normalized Nd PL from Nd doped silica (Nd:Silica), amorphous bulk silicon containing carbon (Nd:aSiC), bulk amorphous hydrogenated silicon (Nd:aSi<H>), and amorphous porous silicon (Nd:apSi), modified after [4], [5], and [6] are shown on the same axis. . . . .	61
6.2	Model of amorphous Si nanocluster to Nd ion energy transfer. . . . .	68
6.3	Nd and amorphous Si nanocluster PL as a function of temperatures, along with a fit to the Nd PL data from Eq. 6.11 and the fit to the Si PL data from equation 6.10. . . . .	71
D.1	photon counter block diagram. The discriminator selects the minimum signal voltage of one count, counted after the trigger voltage is applied. . . . .	86

Acronym	Definition
AOM	Acousto-Optic Modulator
BPF	Band-pass filter
CCA	Crystalline Colloidal Arrays (photonics)
CCD	Charged Coupled Device
CW	continuous wave
EMPA	Electron Microprobe Analysis
LPF	Long-pass filter
nc	nanocluster
Nd:SiO <sub>2</sub>	Neodymium doped silicon dioxide
Nd:silica	Neodymium doped silica
Nd <sub>2</sub> O <sub>3</sub>	Neodymium oxide
OOI	Ocean Optics Incorporated
PL	Photoluminescence
PMT	Photomultiplier Tube
RE	Rare Earth
TEM	Transmission electron microscope
YAG	Yttrium Aluminium Garnet
Symbol	Definition
$E$	Energy
$I$	intensity
$\hbar$	Planck's constant divided by $2\pi$
$R^2$	coefficient of determination of a linear regression
$R$	excitation rate
$r$	radius from thermal evaporation point source
$w$	rate
$x$	horizontal distance from thermal evaporation point source
$\Delta a$	radius of localization (due to quantum confinement)
$\Delta E$	energy difference
$\Delta y$	vertical distance from thermal evaporation point source
$\theta$	angle
$\beta$	constant exponent of a stretched exponential, is a measure of 'stretch'
$\Phi_{phot}$	photon flux
$\tau$	1/e time constant
$\sigma_{eff}^{Nd^{3+}}$	effective cross-section

# Chapter 1

## Motivation

The intra- $4f$  shell transitions of the rare earth (RE) ions have a variety of attractive luminescence properties [7, 8, 9, 10]. This luminescence can occur throughout the visible spectrum and into the near infrared, depending on the rare earth and the specific transition involved. Local electric fields due to the host material induce a mixing of states of opposite parity in the dopant RE ions, weakly allowing transitions within the  $4f$  shell [11]. However, because these transitions are normally forbidden by selection rules (Section 2.1), the absorption cross-sections for the transitions (e.g., for optical excitation) are low, generally on the order of  $10^{-21}$   $\text{cm}^2$  (eg. Er [12, 13], Nd [14]). The parity forbidden transitions result in long lifetimes of the excited ions (e.g. on the order of a few milliseconds for Er in glass [11]), an important characteristic for population inversion in rare earth lasers which require excited state lifetimes greater than several hundred  $\mu\text{s}$  [15]. Also, the  $4f$ -shell electrons [16], are screened by the outer shell electrons [16] such that the spectral dependence on the surrounding matrix is weak. These characteristics are further discussed in Section 2.1.

The luminescent transitions of the rare earths have extensive applications in optical communications, and a very brief description of some of these applications can serve as illustrations of the value of (and problems associated with) the luminescence of the rare earths. For example the 1980s saw the advent of erbium doped fiber amplifiers for amplification of optical signals at  $\sim 1.5 \mu\text{m}$ , one of the minimum attenuation bands for silica fibers (eg. [17, 18], Fig. 1.2). In these devices the Er doped silica fiber is pumped (typically by a 980 nm laser) which

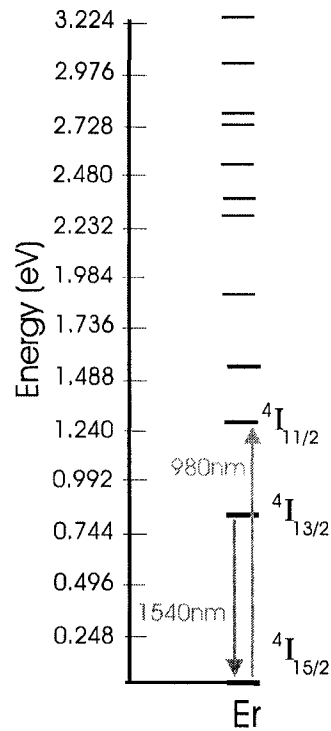


Figure 1.1: The lower 4f-shell energy levels of an Er ion.

excites an erbium electron to the  ${}^4I_{11/2}$  state (Fig. 1.1). After  $\sim \mu\text{s}$  an electron decays non-radiatively from the  ${}^4I_{11/2}$  state to the first excited state,  ${}^4I_{13/2}$ . The final radiative transition to the  ${}^4I_{15/2}$  ground state occurs with the emission of a  $\sim 1530$  nm photon [11].

The low excitation cross-section and non-radiative transitions of the free carriers result in low output power of a typical RE optical amplifier [17, 19]. There are two main approaches to increase the output power: an increase in pump flux, and an increase in the number of erbium ions. The Er absorption cross-section is highest at 980 nm where there is a narrow absorption band [19]. Because of the narrow absorption band the amplifier typically requires a wavelength-stabilized pump laser with high pump flux [19], which is generally expensive. The second approach, to increase the number of rare earth ions available to be excited, may be achieved by increasing the Er concentration or increasing the interaction volume of the fiber. The total Er concentration is limited by concentration quenching effects

(see Chapter 2.5), whereby the efficiency of the system decreases after a threshold Er concentration [20, 21]. An increase in volume can be achieved by increasing the length, however, lengths on the order of tens of meters are typically required to achieve a significant amplification [18]. The long fiber length, as well as being potentially bulky, increases the attenuation in the fiber due to scattering and is unsuitable for erbium doped waveguide amplifiers, which must be short. These pump laser and size restrictions make Er doped silica impractical for waveguide amplifiers.

In the mid-1990s, silicon nanocrystals (with radii on the order of several nanometers) embedded in a matrix of  $\text{SiO}_2$  were found to be excellent sensitizers for erbium ions [22, 23]. Effectively, the silicon nanocrystals absorb incident radiation and transfer the resulting carriers to nearby erbium ions through a much-debated, but as-yet uncertain, mechanism [24]. The two most frequently used models to explain the transfer are dipole coupling [25], and non-resonant excitation of the erbium ions [26]. The non-resonant mechanism dominates in Si nanocluster systems (both amorphous [3] and crystalline [27]), with a coupling efficiency close to unity [28, 29]. The resulting excitation cross-section is approximately 4-5 orders of magnitude greater compared to direct pumping of the rare earth ions, and can be approximately equal to the absorption cross-section for the nanoclusters,  $\sim 10^{-16} \text{ cm}^2$  [30, 31]. The high excitation cross-section for erbium in silicon nanocrystal glasses has led several researchers to suggest the possibility of fabricating erbium doped waveguide amplifiers (EDWA), and signal enhancement has been reported recently in waveguide geometries [32].

Despite the level of research in erbium doped silicon nanocrystals there has been only a small number of studies on other technically important rare earths, such as ytterbium, terbium, and neodymium. Neodymium is of interest because of its emission band in the second optical fiber transparency window (Fig. 1.2), and because of its role in doped ceramics as a classic laser medium. Furthermore, our group recently reported that *amorphous* silicon nanoclusters can act as the sensitizers for Er ions [3], leading to the prediction that Nd might show an a similar effect. The low processing temperature (on the order of a few hundred degrees) required for the amorphous silicon nanoclusters is compatible with complementary metal oxide semiconductor (CMOS) devices, in contrast to silicon nanocrystals

which require thermal processing temperatures of 1000°C or more. This makes amorphous nanoclusters attractive for potential applications (eg. [31, 33]).

Two applications of Nd-doped materials in which the addition of Si nanoclusters may be an advantage are fiber amplifiers and Nd-doped solid state lasers. Amplifiers are required to maintain signal strength over long distances ( $> 100$  km) in fiber optics [34]. Of the three principal windows in previously laid fused silica optical fiber the transmission window at 1312 nm is not exploited to its full potential due to the absence of an appropriate optical amplification medium at this wavelength. Currently, amplification of 1300 nm signal relies on electro-optical conversion, which introduces electrical noise to the signal and restricts the maximum data transfer rate to 40 Gb/s [35]. An all-optical system, on the other hand, could have transfer rates of upwards of 100 Gb/s [35]. The  ${}^4F_{3/2} \rightarrow {}^4I_{13/2}$  Nd PL falls within this transmission window, however the excitation cross-section is low. Coupled with Si-nanoclusters the efficiency of such an amplifier may be increased specifically due to larger excitation cross-sections and the ability to pump with white light. At present the photoluminescence (PL) of this transition is too weak due to the low branching ratio of the  ${}^4F_{3/2} \rightarrow {}^4I_{13/2}$  for first generation fiber amplifier applications.

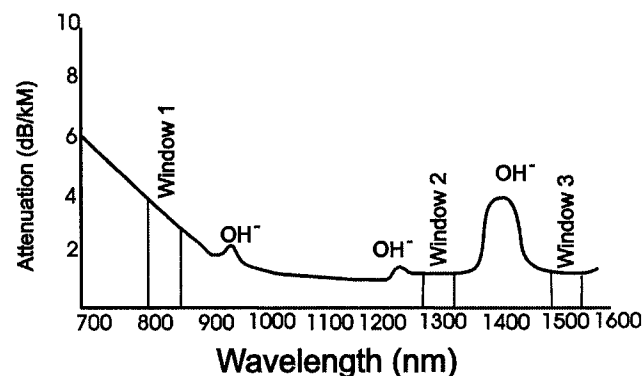


Figure 1.2: The variation of attenuation in silica optical fibers with wavelength. The three principal windows of operation are indicated and ‘OH<sup>-</sup>’ symbols indicate increased attenuation due to the presence of hydroxyl radicals in the cable material. Adapted after [2].

Neodymium is the most common dopant used in a variety of solid state laser



host materials [15]. Generally the highest gain of these Nd doped materials is near 1060 nm [36], but lasing near 900 and 1300 nm has also been reported (see Section 2.1). The efficiency and output of Nd:crystal lasers are generally limited by the low Nd absorption cross-section [15], necessitating large, often difficult-to-grow crystals with high concentrations of Nd. The concentration of Nd is limited by concentration quenching which causes a decrease in the upper lifetime of the system (see Section 2.5), as in the case of Er. Here, again, an increased effective excitation cross-section would increase the efficiency of a Nd laser. The potential deleterious effects of silicon nanoclusters for these applications (e.g. confined carrier absorption) have not been widely investigated.

From the point of view of fundamental physics (interactions of amorphous Si nanoclusters with RE ions) and potential future devices (amplifiers, silicon-based lasers) these materials are of current interest. It is clear that Nd has important optical applications, similar to those of Er but at different key wavelengths. An increase in the effective excitation cross-section in an easy-to-synthesize medium with low processing temperatures is technologically relevant, while the energy exchange between the Si nanoclusters and Nd-ion is interesting on a fundamental level. The goals of this study were therefore as follows: a) to determine whether amorphous silicon clusters can sensitize the optical transition in neodymium, b) to determine the optimal conditions under which the Nd luminescence is maximized, c) to investigate the dynamics of the Nd luminescence and compare the results with traditional Nd laser glass, d) to probe the amorphous Si-nanocluster - Nd interaction mechanism and estimate the relevant cross-sections, and e) to provide a preliminary evaluation of the possibility for optical gain from Nd in Si-nanocluster glass.

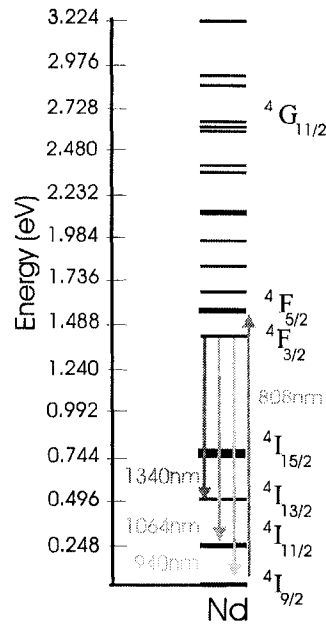
# Chapter 2

## Background

### 2.1 Nd electronic configuration and transitions

Neodymium is a trivalent rare earth: a group of metals comprised of three members of Group IIIB and 14 lanthanides. These are: scandium (21), yttrium (39), lanthanum (57), cerium (58), praseodymium (59), neodymium (60), promethium (61), samarium (62), europium (63), gadolinium (64), terbium (65), dysprosium (66), holmium (67), erbium (68), thulium (69), ytterbium (70) and lutetium (71). The ground state of the electronic configuration of the rare earths can be written as  $[\text{Pd}]4f^{\#}5s^25p^6$ . Because of their electronic structure, they commonly form stable compounds where their valance is +3 (e.g. oxides or borides), and only occur as such compounds in nature (exceptions include Ce, Pr and Tb, which also exhibit +4, and Sm, Eu, Tm, and Yb which also exhibit +2). As the atomic number increases, electrons are added to the  $4f$  orbital. These  $4f$  electrons are responsible for the luminescent properties of the ion and are largely screened from their environment by the outer orbitals.

As a free ion the RE transitions between  $4f$ -shell energy levels are parity forbidden because of the selection rules. However, when in a solid host the electrostatic and spin interactions split the electron configuration into multiplets, and the crystal field further splits these into crystal field components [16, 11]. This induces a weak mixing of states of opposite parity, and results in many energy levels with parity-forbidden optical transitions weakly allowed between states belonging to the same  $4f$  ground-state electronic configuration [11]. Many excited states are

Figure 2.1: Energy levels of Nd<sup>3+</sup>.

‘meta-stable’ because the transitions are technically forbidden and therefore have lifetimes on the order of 10-100 ms in the visible range [37], and 0.1-10 ms in the infrared range [1]. Because these transitions are only weakly allowed the optical excitation cross-section is very small, on the order of  $10^{-20}$  cm<sup>2</sup> [21].

The Nd<sup>3+</sup> energy levels are affected by their local environment, however the 4f electrons (responsible for the atom’s optical properties [16]) are largely screened from their environment by the filled  $5s^25p^6$  outer shells [16]. The weaker crystal field interaction of the 4f electrons reduces electron-phonon coupling [16] resulting in narrow luminescence bands (e.g. 1 nm linewidth of Er  $4I_{13/2} \rightarrow 4I_{15/2}$  luminescence at low temperatures in crystalline Si [38]). The outer shell also largely screens the ligand field of the matrix, making the emission energies largely (but not entirely) independent of the host material. Variations in the environment do cause slight changes in the optical characteristics of neodymium (Table 2.1). For example, the energy gap between  $4F_{3/2}$  and  $4I_{11/2}$  is slightly greater in amorphous Nd:glass (1.176-1.167 eV) than crystalline Nd:YAG (1.165 eV). The disordered environment in glass increases the PL linewidth by almost a factor of 60 compared

to that in crystal (i.e. the linewidth of the  ${}^4F_{3/2} \rightarrow {}^4I_{11/2}$  luminescence increases from 0.45 nm to 18-28 nm [15]). The radiative lifetime also increases, eg. the  ${}^4F_{3/2} \rightarrow {}^4I_{11/2}$  PL decay time increases from 230  $\mu\text{s}$  in crystal to 320  $\mu\text{s}$  in glass [15].

The photo-excitation and subsequent radiative decay of a Nd ion are described here. The first few energy levels of a neodymium ion in a solid host are shown in Fig. 2.1. The  ${}^4I_{3/2} \rightarrow {}^4F_{5/2}$  absorption has an excitation cross-section at 808 nm of  $\sim 10^{-23}\text{cm}^2$  [15]. An electron decays non-radiatively from the  ${}^4F_{5/2}$  state to the meta-stable  ${}^4F_{3/2}$  state [15]. From this excited state an electron may decay radiatively to the  ${}^4I_{13/2}$ ,  ${}^4I_{11/2}$ , or  ${}^4I_{9/2}$  levels, corresponding to PL intensity peaks centred around 1338, 1064, and 940 nm respectively [10, 15] (Fig. 2.1). The gap between the terminal states  ${}^4I_{13/2}$  or  ${}^4I_{11/2}$  and the ground state ( ${}^4I_{9/2}$ ) is  $\sim 0.5$  eV or 0.25 eV respectively. These levels therefore have negligible populations at 300 K, and the relaxation into the ground state is fast and non-radiative [15]. This precludes any population buildup, making the 1060 and 1300 nm transitions true 4-level operations. The  ${}^4F_{3/2}$  gain can be reduced by excited state absorption at 1300 nm, whereby an excited ion may be further pumped by an incoming photon to a  $4g$  level. The electron in this new level may not decay with the same mechanism if there are other paths available to it, and so the desired fluorescence can be lost.

The interaction of Nd ions with silicon nanoclusters has been studied very little; therefore, in order to understand the way a rare earth ion can interact with silicon it is necessary to look at the specific case of erbium, for which there is an abundance of data. Presented here is a very brief look at the interactions of Er with bulk silicon, silicon nanocrystals, and amorphous Si nanoclusters. Although this summary is necessarily short, the reader will be referred to many seminal references in case more detailed information is required.

## 2.2 Er in Silicon

Electronic transitions in bulk Si can include inter-band and intra-band transitions, and energy transfer between impurities and bands. Band-to-band transitions, due to the absorption of photons at energies above the bandgap, create electron-hole pairs in the Si [39] (Appendix A). An electron-hole pair in bulk Si has a very

Glass	$\sigma$ of peak ( $10^{20}\text{cm}^2$ )	$\tau_{1.06}$ ( $\mu\text{s}$ )	$\tau_{all}$ ( $\mu\text{s}$ )	$\tau$ $\tau_{1.06}$
Kodak Nd11	2.35	950	360	0.26
Schott LG55	1.22	1960	600	0.34
Chance-Pilkington LN6	1.3-2.1	1850	450	0.24

Table 2.1: 1.06  $\mu\text{m}$  peak of Nd photoluminescence in various host glasses.  $\sigma$  is the cross-section,  $\tau_{1.06}$  is the lifetime of the Nd  ${}^4F_{3/2} \rightarrow {}^4I_{11/2}$  transition centred at 1060 nm, and  $\tau_{all}$  is the total radiative decay time of the system (measured over all transitions). Modified after [1].

low probability of recombination due to the indirect bandgap. Recombination requires a third body to satisfy the conservation of momentum (e.g. a phonon), which results in a long carrier lifetime (60  $ms$  at low temperature [40]). A defect (e.g. neutral donor introduced by Er [41]) present in the crystal can introduce a localized mid-gap state i.e. a lower electronic energy state ( $\sim 3$  meV for shallow donors such as Er [40]). An electron-hole pair trapped at a defect state is localized, which relaxes the momentum constraint via the uncertainty principal and therefore increases the probability of recombination. The lifetime of the electron-hole pair trapped in the defect level is on the order of a few microseconds [40].

Er can be excited to its  ${}^4I_{13/2}$  or higher state by an Auger process from an electron-hole pair trapped at a defect level [26] (Fig. 2.2). The Auger effect is a non-radiative process, whereby an excited electron transfers energy to an Er electron (Auger electron). The energy transferred corresponds to the difference between the initial transition energy and the ionization energy of the Auger electron. Excess energy due to the energy mismatch of Si and Er excited states is absorbed by free electrons or phonons. Er in silicon exhibits a significant increase in the excitation cross-section with indirect excitation ( $\sigma_{eff} \sim 5 \times 10^{-12} \text{ cm}^2$  [41]) compared to direct excitation of Er in an insulating host ( $\sigma_{eff} \sim 10^{-21} \text{ cm}^2$  [41]) due to these processes [26].

Er doped silicon is characterized by strong temperature quenching [26, 42] due to an Auger processes in which energy of the excited Er is transferred back to the Si, exciting an electron above the bandgap (the reverse of the process in Fig. 2.2, [42]). Due to phonon emission for energy conservation, the new electron-hole pair

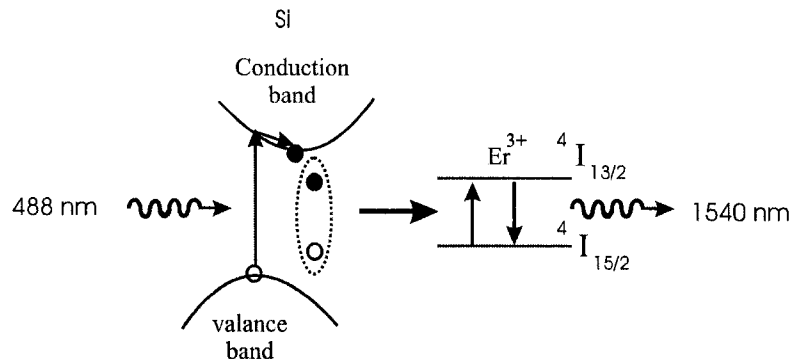


Figure 2.2: Model of Er doped crystalline Si. Phonon-assisted Si excitation creates an electron-hole pair which subsequently excites an Er ion through Auger process.

generally has less energy than the electron-hole pair that initially excited the Er. The pair therefore may not be energetic enough to excite another Er, resulting in a net loss of Er luminescence [26].

At high concentrations non-radiative effects dominate [20, 21]. The average distance between Er ions decreases as the concentration increases and therefore electric dipole-dipole interactions between ions becomes more significant [43]. An excited Er electron may resonantly transfer its energy to excite another nearby Er ion [44]. This Er-to-Er excitation migration is not detrimental in itself, however a number of ions may be coupled to quenching sites (e.g. -OH groups [44]). As the probability of ion-ion transfers increases, the likelihood of exciting an ion coupled to a quenching site increases. Once quenched, the excitation is lost [44] so the Er luminescence is decreased.

### 2.3 Er in Si-nanocrystal systems

Silicon is the leading semiconductor in microelectronics, however its indirect band gap and lack of linear electro-optical effects (changes in absorption, refractive index) make it unsuitable for optoelectronic applications. By reducing Si from bulk to nano-scale particles the electronic characteristics are altered due to quantum size effects [45].

In brief [45], when one or more of the crystal dimensions decreases to approx-

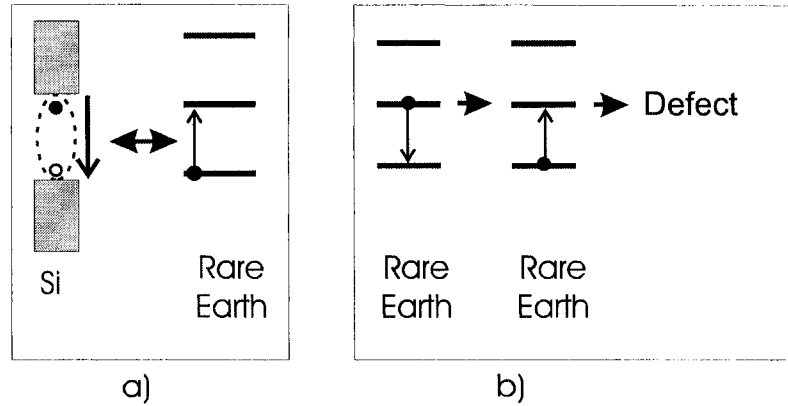


Figure 2.3: Non-radiative processes in Er-doped Si nanocrystals: a) Auger processes from nanocrystal to rare earth and from rare earth to nanocrystal, b) Migration and defect quenching.

imately the size of the exciton Bohr radius ( $a_B$ , approximately 4-5 nm in bulk Si) the carriers are in the quantum confinement regime. The carriers are confined by barriers associated with the crystal-host boundary. A carrier confined in one dimension is in a quantum well, confined in two dimensions it is in a quantum wire, and confined in all three dimensions is in a quantum dot. The change in electronic properties from bulk to nanocluster is continuous [46] (for a more complete description see Appendix B). In the nanoscale range there are two regimes: the weak confinement regime, where the cluster radius ranges from approximately two to several times larger than  $a_B$ ; and the strong confinement regime, where the radius is much less than  $a_B$ . Both regimes display a decrease in energy of the ground state of the electron-hole pair with increasing particle size (Appendix B), therefore, as particle size decreases the emission energy due to pair recombination increases.

In bulk crystal the density of states increases away from the band gap ( $\propto \sqrt{E}$  where  $E$  is energy, Appendix A). In the 1- and 0-D systems the density of states is greatest near the sub-band edges ( $\propto 1/2E$ ) or entirely confined to the elementary energy levels (at  $\delta_{E-E'}$ ) respectively. This results in a narrower emission linewidth, as most of the transitions occur at or near the sub-band edges. The carrier localization due to quantum confinement (localization radius of  $\Delta a$ ) reduces

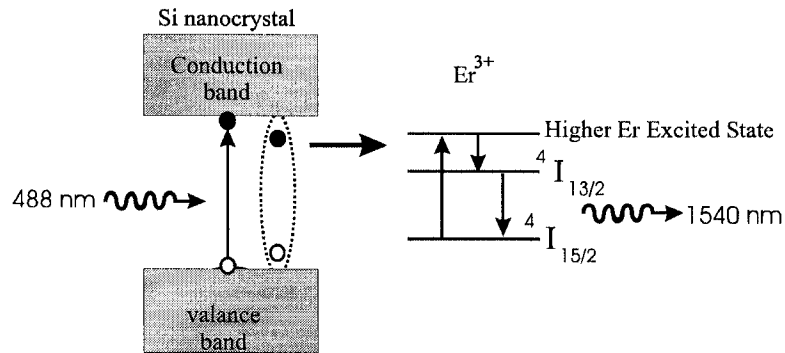


Figure 2.4: Model of Er Förster excitation of Er by an excited crystalline Si nanocrystal.

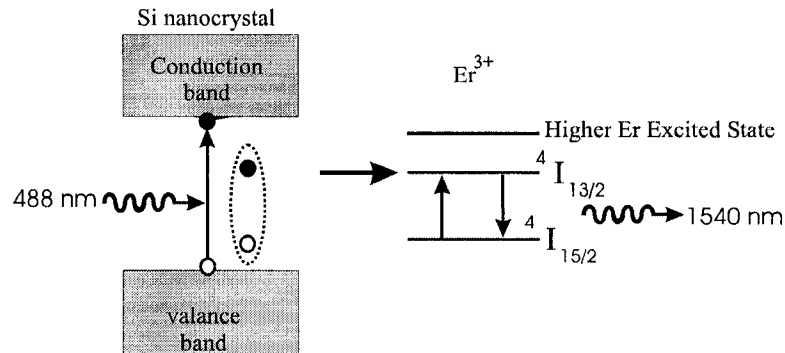


Figure 2.5: Model of Er Auger excitation Er doped  $\text{SiO}_2$  containing crystalline Si nanoclusters.

the momentum constraint on transitions ( $\Delta a \Delta p \geq \hbar/2$ , where  $p$  is momentum). This can result in a more direct band gap which no longer requires a phonon during excitation/de-excitation and therefore increases the rate of recombination.

One method to produce the Si nanocrystals is to deposit several hundred nanometers of SiO on a  $\text{SiO}_2$  substrate, followed by thermal processing. SiO, a thermodynamically unstable compound at room temperature, begins to phase separate into  $\text{SiO}_2$  and Si at temperatures above  $300^\circ\text{C}$  [47, 3]. During phase separation the Si separates out and forms clusters, leaving behind non-stoichiometric amorphous  $\text{SiO}_x$ . The  $\text{SiO}_x$  approaches a composition of  $\text{SiO}_2$  with increasing phase separation [47]. At temperatures below  $900^\circ\text{C}$  [47] the nanoparticles are



amorphous clusters [3], above 900°C they are crystalline. Er-doped nanocomposites can be achieved by doping these SiO films with Er or Er oxides and thermally processing them.

To obtain Er PL a Si nanocluster is initially excited by a pump laser, creating an electron-hole pair which rapidly decays to a lower energy state [48]. The energy is transferred non-radiatively to the Er, exciting an  ${}^4I_{15/2}$  electron to an upper energy level [30, 46, 41]. An electron in this upper level then quickly decays non-radiatively to the  ${}^4I_{11/2}$  or  ${}^4I_{13/2}$  level [49], and then finally decays radiatively to the ground state with the emission of a 980 or 1540 nm photon. Er in Si-nanocrystal-doped SiO<sub>2</sub> has a reported lifetime of 1 to 2 ms [41, 30].

Two main energy transfer mechanisms have been proposed for the Er with Si nanoclusters: Förster and Auger processes. Förster-type energy exchange involves resonant dipole-dipole interaction between the electron-hole pair and Er. The non-radiative recombination of an electron-hole pair is accompanied by excitation of the rare-earth ion (Fig. 2.4). Time constants for this process have been experimentally determined to be on the order of a few tens of nanoseconds (e.g. [50, 24]). The Förster process is claimed to occur between nanoclusters and RE ions with a separation of more than a nanometer [50, 24].

Auger-type energy transfer, the second energy transfer mechanism proposed for the Er with Si nanoclusters, has been observed in RE doped bulk Si (Section 2.2). Band-to-band absorption in the bulk Si forms an electron-hole pair, which is then captured by a neutral defect introduced by the Er [26]. The pair recombines non-radiatively through an Auger process which transfers the energy to the 4f shell of the Er ion via a Coulomb interaction [26] (Fig. 2.5). Reference [51] has labeled this a ‘fast’ transition, with a time constant of less than a microsecond. This type of transfer is also claimed to occur between nanoclusters and ions with separations of less than a nanometer [51].

## 2.4 Er in amorphous Si-nanocluster systems

The description of Er with *amorphous*, as opposed to crystalline, nanoclusters, is considerably more complex. Calculating the Bohr radius in an amorphous host is more complicated because the effective mass is affected by the local electron/hole

environment [45]. The surroundings of a single ion may be approximated as crystalline in the near-neighbour range, but will differ from site to site. In amorphous silicon, carriers rapidly localize in the band tails [52]. These states have an energy distribution that follows an exponential tail extending from the conduction and valence bands [52]. Radiative recombination can then occur between trapped electrons and holes at an energy below the mobility gap of amorphous silicon [52]. Alternatively, deep non-radiative traps (e.g., dangling bonds) can provide an undesirable non-radiative recombination pathway [52].

Mott [53] has estimated the band tail localization distance to be on the order of 1 nm, meaning quantum confinement would not play a role except in the smallest clusters. However, particle size can affect the emission energy via a statistical blueshift due to the availability of deep levels in the bandgap [52]. As well, quantization of the extended states should play a role in the thermalization of carriers from the band tails back into the mobility gap [52]. This effect might be observable in the temperature dependence of the amorphous nanocluster luminescence since thermalized carriers can recombine non-radiatively. Of particular relevance to the present work, our group has recently demonstrated that these amorphous clusters can be sensitizers for erbium ions, and that the energy transfer process between an amorphous nanocluster and nearby  $\text{Er}^{3+}$  is at least qualitatively similar to the process that occurs in the much more widely-investigated erbium-doped silicon nanocrystal systems [31, 54].

The amorphous silicon nanoclusters grown for this study were produced by annealing an SiO film at temperatures below 800°C in an oxygen deficient environment to induce phase separation of the SiO. Previous studies on similarly-processed un-doped films [3] have included high resolution transmission electron microscopy (TEM) using energy filtered TEM to determine the size and structure of the clusters. The diffraction pattern of the SiO sample annealed at 500°C did not have periodic patterns or rings, indicating lack of long range atomic periodicity. Silicon-rich clusters with radii estimated to be 1-1.5 nm ( $\sim 200 - 1000$  atoms) were observed in the energy filtered TEM images. In contrast, a distinct crystalline structure and well-defined rings in the diffraction pattern were observed for a SiO film annealed at 900°C.

The PL intensity temperature dependence is governed by the same mechanisms

in the bulk and nanocluster amorphous Si [55]. At higher temperatures the number of carriers thermally excited from the bandtail states to the conduction band [55] is increased. From the conduction band they may then be captured by non-radiative recombination centres (due to dangling bonds and structural disorder [55]). The PL intensity of both bulk and nanocluster amorphous Si as a function of temperature is described by  $I_0/I - 1 \propto e^{-T/T_0}$  [56], where  $I_0$  is the intensity at  $T = 0$  (extrapolated from the data), and  $T_0$  is proportional to the Urbach energy and describes the ratio of non-radiative to radiative decay rates. The PL intensity of the nanoclusters is less temperature sensitive than that of bulk amorphous Si [55].

Recently our group achieved Er PL through pumping of the amorphous nanoclusters [33]. Er-doped silicon nanocluster films were grown by co-evaporation of Er and SiO, and thermally processed in 95% N<sub>2</sub> + 5% H<sub>2</sub> environment. Maximum PL intensity for 325 and 476 nm pump wavelengths was observed at an annealing temperature of 500°C and an Er concentration of  $\approx 0.20$  atomic %. The reduction of Er PL at annealing temperatures below 500°C was attributed to the presence of defects [57], which are removed at higher temperatures. The decrease in PL at temperatures greater than 500°C is speculated to be due to Er clustering or oxygen out-diffusion [58]. The effective excitation Er cross-section was determined to be similar to that of crystalline nanoparticles,  $\sim 2 \times 10^{-16}$  cm<sup>2</sup> [33].

## 2.5 Mechanisms of non-radiative recombination

RE ions in a film with amorphous silicon nanoclusters have excitation cross-sections five orders of magnitude larger than that of RE in SiO<sub>2</sub> ( $10^{-21}$  cm<sup>2</sup> for Er [59] and Nd [1] in glass compared to  $10^{-16}$  cm<sup>2</sup> for Er [33] in nanocluster-containing SiO<sub>2</sub>), and can be pumped with white light. Efficiency is limited, however, by energy transfer from nanocluster to excited RE ion, from RE to nanocluster, from RE to RE ion, or by clustering effects (Fig. 2.6). These effects, which can potentially reduce RE luminescence intensity and PL decay times, are discussed in this section.

Nd ions are excited by the transfer of energy from the nanoclusters. If the transfer occurs from an excited nanocluster to a pre-excited RE ion, the RE ion is “doubly excited”. This occurs if there is an appropriate energy level above the RE excited level, where the energy difference between the excited states corresponds

to the energy of the excited nanocluster. This effect is more pronounced at high pumping rates ( $\sim 100$  mW for Er [60]).

The same process that transfers energy from the nanocluster to RE ion may also occur in reverse, exciting a nearby nanocluster through the non-radiative de-excitation of the RE ion [61]. Phonon interactions are required for energy conservation during the ‘back-transfer’ process [50, 61], therefore this transfer plays a major role in the temperature quenching of RE PL [50, 61]. An effect related to the back-transfer process occurs when energy is transferred from an excited RE to a pre-excited nanocluster. Because it relies on a large number of RE ions being pre-excited, this ‘impurity Auger process’ is stronger at high pump power. Back-transfer and impurity Auger processes may be reduced in RE-doped crystalline semiconductors by increasing the energy barrier (energy mismatch between the electron-hole pair and RE ion) [24]. An increased energy-barrier can be achieved by increasing the band gap through quantum confinement effects (i.e. changing the semiconductor, or decreasing nanocluster size) [24]. However, according to Taniguchi *et al.* [8] the energy mismatch between the  ${}^4F_{3/2} \rightarrow {}^4I_{9/2}$  transition energy (1.35 eV) and the phosphorous band gap (2.26 eV) was not enough to prevent back-transfer. They concluded that though the energy barrier is a factor in the suppression of temperature quenching due to energy transfer from the excited RE to nanoclusters, it is not the only source. Seo *et al.* suggested that nanocluster-to-RE separation is at least as important as the band gap increase [62]. An increased separation generally leads to a weaker coupling strength which reduces the probability of transfer both from the RE to a nanocluster, and also from the nanoclusters to the RE. This effect would apply to both the crystalline and amorphous nanocluster systems.

At high RE concentrations, where the RE-RE separation decreases, RE-RE interactions tend to dominate [20, 21, 36]. The strength of the dipole interaction varies inversely with the distance between RE ions to the sixth power [36]. Along with the RE-RE separation, the probability of interaction depends on the host material (dielectric constant, typical phonon energy), the exact energy levels and cross-sections, concentration, and spatial distribution of the RE ions. Excitation diffusion, introduced in Section 2.2 (Fig. 2.3 b), is the non-radiative de-excitation of an excited RE ion by resonant energy transfer to a second, unexcited ion (Fig.

2.7). This transfer from ion to ion continues until an ion decays radiatively or the excitation is transferred to an ion coupled to a quenching site [63], the latter resulting in an increased PL decay rate accompanied by a net loss of PL. This effect depends on the number of quenching sites, and would therefore be reduced by reducing the number of impurities or defects with energy levels resonant with the RE levels.

Co-operative up-conversion, another concentration-dependent quenching process [9], is the de-excitation of an excited RE ion through non-radiative energy transfer to a neighbouring pre-excited RE ion, exciting a carrier of the second ion to an upper energy level approximately twice the energy of the initially excited state [9, 20]. Because this effect depends on the number of excited RE ions it is therefore more effective at high pump rates. In Er doped  $\text{SiO}_2$ :Si-nc samples these concentration quenching effects are dominant at Er concentrations above  $10^{19}$  to  $10^{20} \text{ cm}^{-3}$  [60].

Clustering occurs at higher RE concentrations. The clustering of Nd, as well as all other RE ions, is due in part to the large cationic field strength. The electric charge of the cation is screened by non-bridging oxygens, e.g. in silica glass [21]. The  $\text{SiO}_2$  network is too rigid to allow sufficient coordination of oxygens to sufficiently screen the charge, therefore the Nd ions may cluster to reduce enthalpy by sharing the non-bridging oxygens [21]. The critical concentration at which this effect begins to occur for Nd in  $\text{SiO}_2$  glass has been estimated to be  $1 \times 10^{19} \text{ cm}^{-3}$  [64]. Introduction of impurities such as aluminium and phosphorous have been shown to increase the critical concentration by reducing the rigidity of the bonding configuration [21]. Such dopants are frequently used in laser glasses.

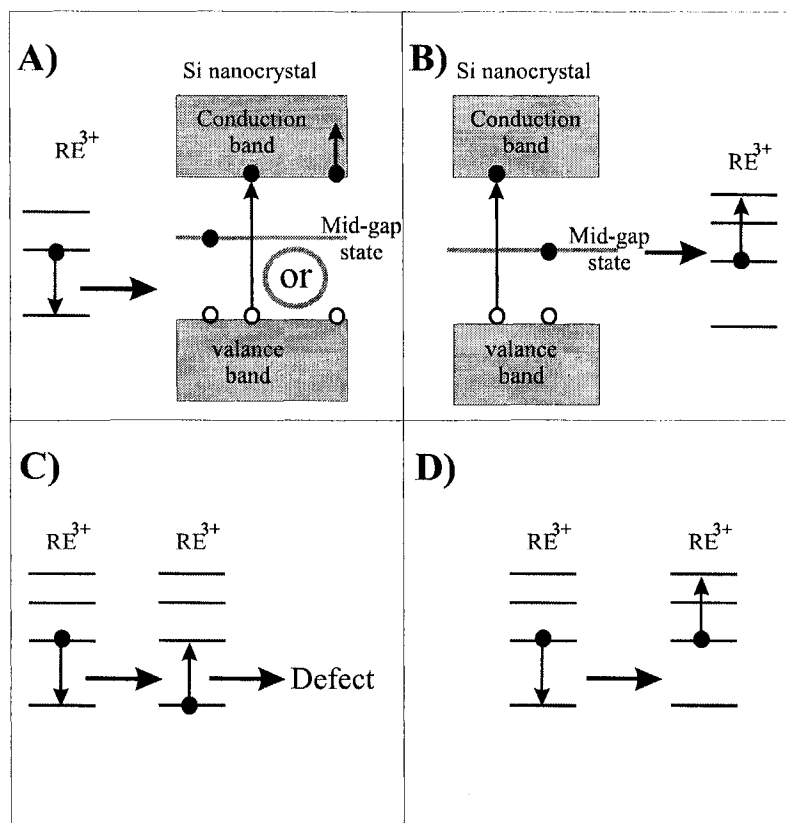


Figure 2.6: Mechanisms of non-radiative recombination in the RE-doped silicon nanocluster glass include A) back transfer (left), or impurity Auger excitation (right), B) second excitation of an ion into a higher excited state, C) excitation diffusion, and D) co-operative up-conversion.

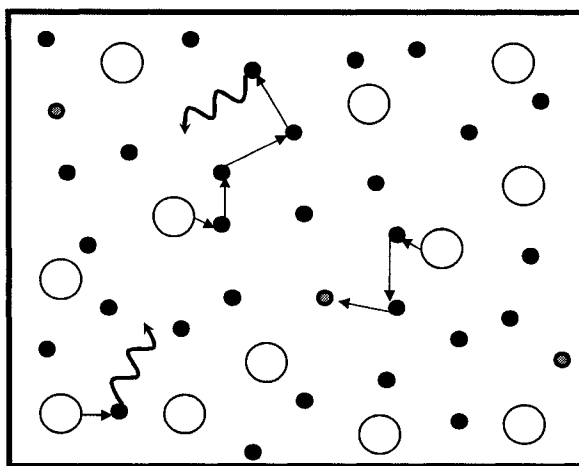


Figure 2.7: Sketch of excitation diffusion. Black arrows are energy transfers, white circles are Si nanoclusters, black circles are Nd ions, grey circles are Nd ions coupled to quenching sites.

## Chapter 3

# Specimen Synthesis

Two methods were used to grow the films, both using concurrent evaporation of SiO and either Nd<sub>2</sub>O<sub>3</sub> or Nd metal in a vacuum chamber. Electron-beam and thermal methods were used for simultaneous evaporation of the two sources, one for each source. The electron gun consisted of an electron-emitting filament, magnets to control the beam, and a water cooled rotating crucible. The copper crucible fit up to 6 different sources and could be rotated to expose a single source to the e-beam allowing for multiple layers to be grown without exposing the film to atmosphere. The source was located ~80 cm from the substrate such that the film thickness was approximately constant over the entire wafer. The thermal system was comprised of a pair of water-cooled posts, copper clamps, and a source boat made of tantalum or tungsten. A current ran through the posts, heating the boat and causing evaporation or sublimation of the source. The adjustable height of the posts allowed the thermal boat to be raised or lowered in order to achieve graduated or uniform thicknesses across the film. The thickness of the film, as well as the deposition rate, was measured by two crystal monitors at the same height as the substrate. The chamber was pumped down to a base pressure of  $\sim 10^{-6}$  Torr. The substrates were shuttered until rates stabilized, then exposed until the desired thickness was achieved. The Nd concentration was varied by sample from 0.144 to 1.72 atomic % (set A and B respectively) in different specimens.



### 3.1 Set A

In the first set of samples the SiO was evaporated thermally from a tungsten baffle box while Nd<sub>2</sub>O<sub>3</sub> was deposited by electron beam evaporation. The baffle box reduced source spitting by obstructing the direct line of sight between the SiO within the box and the wafer, while permitting the vapour to reach the sample. The Nd<sub>2</sub>O<sub>3</sub> source was contained in a tantalum liner. Though supposedly an excellent e-beam source, maintaining the low Nd rates required for the samples ( 0.1 Å/sec) was a continual problem. A tungsten lid with a 3 mm diameter chimney was added to convert the Nd<sub>2</sub>O<sub>3</sub> system to a thermal source, such that the heating element became the tungsten lid exposed to the electron beam. Nd<sub>2</sub>O<sub>3</sub> (density of 7.240 g/cm<sup>3</sup>) is known to lose oxygen during deposition [65], and therefore, because the crystal monitor was recording thickness of a Nd-rich (density of 7.010 g/cm<sup>3</sup>) Nd oxide, the amount of Nd actually present in the film was underestimated, in agreement to subsequent characterization. One 100 nm thick film (as determined by the rate monitor) was grown on a 1 by 1 inch wafer, and later divided into 8 pieces for annealing at separate temperatures.

### 3.2 Set B

In the second set of samples SiO was evaporated by electron beam from a tantalum boat with a tungsten lid to quell source spitting, while Nd metal was evaporated from an open Ta thermal boat. The rates of both sources were more stable and easier to control with this setup. To increase the photoluminescence intensity and provide a thicker film for subsequent characterization the films for this series were 200 nm thick, as determined by the rate monitor.

### 3.3 Graduated concentration sample

The last  $\sim 200$  nm thick SiO:Nd sample grown was a graduated Nd concentration film, the setup is illustrated in Fig. 3.1. The vapour emission density from a point source is angle dependent (density  $\sim \sin^2\theta$ ), and also decreases with increased

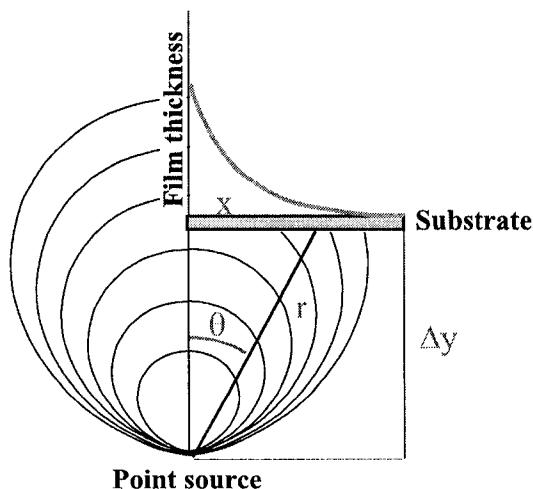


Figure 3.1: Nd deposition set up of graduated concentration sample. Curves are density contour lines of vapour emission. The SiO source was much further away such that the density of vapour emission is considered constant over the film.

distance to the source,

$$r = \sqrt{\Delta y^2 + (x * \cos\theta)^2}, \quad (3.1)$$

where  $r$  is the distance to source,  $\Delta y$  is the vertical source-substrate separation, and  $x$  is the horizontal source-substrate separation. The maximum variation in vapour density with angle occurs near  $45^\circ$ . This setup was tested with a copper source raised to within 15 cm of the substrate. The film thickness of copper determined by simple resistivity measurements, and found to decrease to 1/6 of the maximum over the two three inch wafers (total of six inches). The copper source was replaced by the neodymium source and the graduated neodymium concentration Nd-doped SiO sample was grown under the same conditions as set B. Though the Nd gradient will affect the thickness of the film (on the order of hundredths of a percent) it should not be enough to affect the PL intensity measurably (which, depending on the noise in the baseline of the photoluminescence measurement, varies over a few percent). Using this method the lowest Nd concentration was achieved, extrapolated from the microprobe measurements to be on the order of 0.05 atomic %, below the accuracy of the microprobe for Nd.

### 3.4 Nd doped SiO<sub>2</sub> and Nd doped Silica laser glass

A reference sample of Nd in amorphous SiO<sub>2</sub> was grown under the similar conditions as sample set B, where SiO was replaced with SiO<sub>2</sub> as the e-beam source. The concentration of Nd as recorded by electron microprobe analysis was 0.26 atomic %. In addition, a small Nd doped silica laser glass boule was purchased from Keiger Incorporated. A laser glass is intended to have strong PL with long luminescence lifetimes, therefore the sample has a high concentration of un-clustered Nd, which can be achieved by co-doping with aluminum or phosphorous [21] (Section 2.5).

### 3.5 Film processing

After deposition the films were annealed in a clean furnace at temperatures ranging from 300 to 1100°C in intervals of 100°C with an overpressure of approximately 3 psi of ~ 96% N<sub>2</sub> and ~ 4% H for one hour. The temperature drove the phase separation process that formed the nanoclusters, while the hydrogen was present to passivate Si dangling bonds present in the nanoclusters.

The nucleation and growth of the nanoclusters are diffusion related and have, therefore, a strong temperature dependence [66]. The size of the nanoclusters depends on both the annealing temperature and annealing time. In this study the annealing temperature was varied rather than annealing time to affect both the size and structure (amorphous or crystalline) of the nanoclusters. The microstructure of the silicon clusters annealed over this range of temperatures has been described in a recent publication from our group [67].

## Chapter 4

# Experimental

### 4.1 Electron Microprobe Analysis

Determination of sample composition was done by electron microprobe analysis (EMPA) on the JEOL 8900 microprobe in the Earth and Atmospheric Sciences department. This was necessary to confirm the concentration of neodymium and to test for impurities in the film. In EMPA an accelerated electron beam strikes the film causing an inner shell electrons to be ejected from the atoms in the film. When one of the outer electrons drops to fill the inner shell radiation characteristic of the specific element is emitted. The specimen composition is determined by comparing the specimen x-rays to those emitted by standards of known composition. EMPA probes only the top few microns of the sample, as the penetration depth depends on the accelerating voltage applied to the electrons. The thin films, 100 to 200 nm thick, necessitated the use of low accelerating voltages. The penetration depth of the electrons is roughly

$$d \approx \frac{0.1V_a^{1.5}}{\rho} \mu m, \quad (4.1)$$

where  $V_a$  is accelerating voltage in keV, and  $\rho$  is density in  $\text{g/cm}^3$ . Using Eq. 4.1 for a  $0.2 \mu\text{m}$  SiO sample ( $\rho = 2.432 \text{ g/cm}^3$ ) the accelerating voltage should be less than 3 keV (a Monte Carlo electron-trajectory simulation was done to determine voltage more accurately). This is less than half of the binding energy of the lowest-energy L-shell of neodymium, and therefore the M lines were probed with a 3 kV beam. The x-rays were collected for both energy dispersive spectroscopy (EDS)

and wavelength dispersive spectroscopy (WDS).

In EDS analysis the x-rays struck a single semiconductor crystal and created electron-hole pairs, which were accelerated by a bias across the crystal to create a charge pulse. The number of pairs was determined by the energy of the incident x-rays, and therefore the energy of the x-rays was determined by analyzing the pulse energy. EDS analyzes all emitted x-rays simultaneously and therefore completes a spectrum in several minutes, but because the resolution is only on the order of  $\sim 100$  eV it was used for initial surveys only.

WDS analysis, on the other hand, takes several hours to complete. The  $M_\alpha$  x-rays were collimated and irradiated a thallium acid phosphate (TAP) crystal. The crystal was part of a monochromator and diffracted the photons according to Bragg's law. The x-ray spectrum was scanned by a proportional counter in small increments for a fixed integration time. The low intensity of the  $M_\alpha$  line necessitated the use of longer integration times and decreased the signal-to-noise ratio for the Nd signal. Though WDS takes much longer than EDS the detection limit is lower and the resolution is on the order of  $\sim$  eV, therefore WDS was used in detailed measurements.

The minimum detectable Nd atomic concentration by WDS analysis was  $\sim 0.1$  atomic %. The standards used were  $\text{SiO}_2$  and  $\text{NdPO}_4$  from the Smithsonian Institute. Since the X-ray intensity also depends on the specimen composition some systematic error is expected in the ZAF correction (corrections for atomic number, absorption and fluorescence) technique from comparing a phosphate ( $\text{NdPO}_4$ ) to a silicate (Nd doped  $\text{SiO}$ ).

## 4.2 Optical studies

The optical properties of the sample were characterized by both wavelength and time resolved photoluminescence. All measurements were taken in a closed room with the lights off. The samples were probed by a HeCd or Ar-ion laser, or exposed to a mini deuterium tungsten light source (mini-D2T) with a wavelength range from UV to near IR, and the resulting signal collected by an optical fiber. The signal was measured using a variety of charge coupled device detectors (Table 4.1), or a photomultiplier, and the data analyzed using one of two computer programs.

Detector		Range (nm)	Resolution (nm)
USB2000	USB2G3929	350 - 1000	0.27
USB2000	USB2E2877	550 - 1100	0.27
NIRADC	NIRD118	900 - 1700	1.74

Table 4.1: Spectrometers used in wavelength resolved photoluminescence measurements.

### 4.2.1 Absorption and transmission

To probe the film transmission (and indirectly its absorption) measurements were taken using a mini-D2T light source with a  $\sim 200$  to 1100 nm emission spectrum to illuminate the sample and USB detectors to record the transmitted light. The films were deposited on quartz microscope slides, therefore the measurements were normalized with an identical blank quartz slide. To set up and normalize the detector the mini-D2T was connected to an optical fiber which directed the light to the slide, with the fiber end approximately 1 mm from the slide surface (Fig. 4.1). A second collection fiber was located opposite the source fiber, the collecting end  $\sim 1$  mm from the surface. The collected light was directed to the USB2E2877 spectrometer via the optical fiber, and the position of the fibers adjusted for maximum signal according to the spectral recording of the Ocean Optics Incorporated (OOI) spectrometer operating software. This signal was recorded as having 100 % transmission, and the blank quartz slide replaced with a sample film with the film side towards the source fiber. The results were displayed by the absorption/transmission functions in the OOI spectrometer operating software.

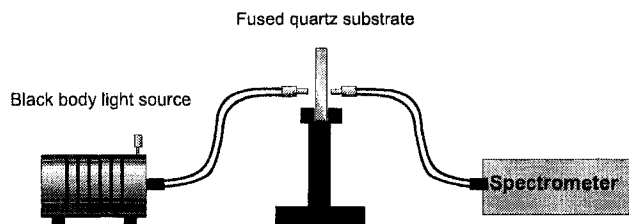


Figure 4.1: Absorption and transmission setup.

### 4.2.2 Wavelength-resolved PL

The spectrometers were normalized with a black body light source, and the spectrometer noise level was established (by subtracting the spectra recorded with the laser shuttered from the spectral data) before each set of measurements. An Ar-ion and HeCd continuous wave (CW) laser were used to pump the samples over a total of ten different wavelengths (Table 4.2) in the wavelength-resolved PL measurements. The HeCd laser output contained both the 325 and the 442 nm lines with a fixed power output of  $\sim 18$  mW at 325 nm, and  $\sim 60$  mW at 442 nm as measured by a power meter just before the sample holder. The wavelengths of the Ar-ion laser were selected within the laser cavity by adjusting an internal mirror and prism, and the optical power used ranged from a few mW to 2 W as determined by an internal power meter. A constant power was automatically maintained by current adjustments. The beam spot on the specimen was a few millimeters in diameter, as estimated by eye at the sample site. The majority of steady state measurements were taken with the strong 476 nm Ar-ion line.

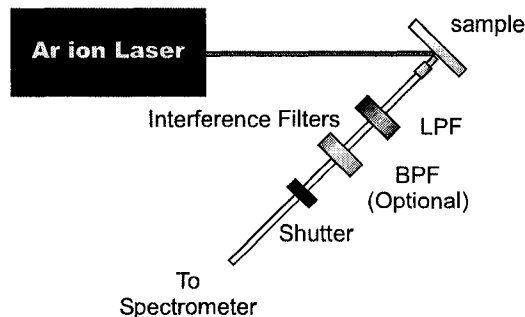


Figure 4.2: Wavelength resolved PL setup.

All the steady state PL measurements were taken with the same setup, as illustrated in Fig. 4.2. The HeCd or Ar-ion laser beam impinged at approximately  $45^\circ$  from the face of the sample, and the PL was collected from a fiber a few millimeters away normal to the sample surface. The collected PL passed through a long-pass filter to prevent laser light from entering the spectrometer, and through a band pass filter to select PL bands (Table 4.3 and Fig. 4.3). The PL data were analyzed using the irradiance function of the OOI software, which displayed the normalized data in bins of about 0.3 or 1.7 nm (Table 4.1).

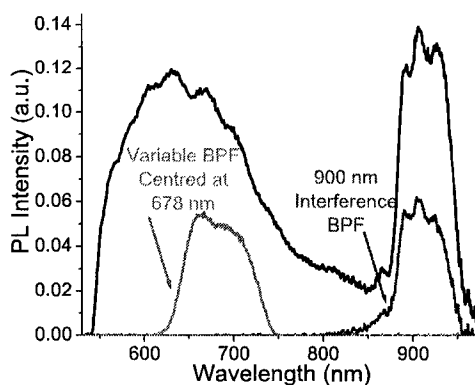


Figure 4.3: PL of a low Nd concentration sample with interference filters. PL bands recorded during time-resolved PL measurements are shown by the blue (Nd) and red (Si-nc) lines, along with the PL spectra recorded with only the 550 nm BPF in black.

### 4.2.3 Time resolved PL measurements

The dynamics of the Nd and Si nanocluster PL were probed using time resolved spectroscopy. The 476 nm line was used to excite the nanoclusters, as it is not resonant with any neodymium transitions (see Fig. 2.1). A low pump power (flux  $\sim 10^{18}$  ions  $\text{cm}^{-2}$ ) was used to ensure the PL remained in the linear response regime (co-operative up conversion of the Nd, excited state absorption of the nanoclusters, and other pump-related non-radiative effects are reduced, see Section 2.5). Power was adjusted at the Ar laser and read off of the laser internal power meter. The actual power reaching the sample is less in AOM measurements than that recorded at the laser aperture by the internal power meter due to the collimating optics.

The CW Ar-ion laser was passed through a series of focusing and collimating optics before reaching the acousto-optic modulator (AOM), which was driven by a tunable function generator (Fig. 4.5). The AOM produced a square pulse with 50% duty cycles to record the PL rise/decay signal (Appendix C). A single mode from the AOM (the first or second mode) was selected by a 1 mm diameter collimator to pump the sample. The pump signal had a rise and fall time on the order of 50 ns (Fig. 4.4). The PL was passed through two interference filters: a 550 nm long pass filter (LPF) to prevent laser light from entering the fibers, and either the 678



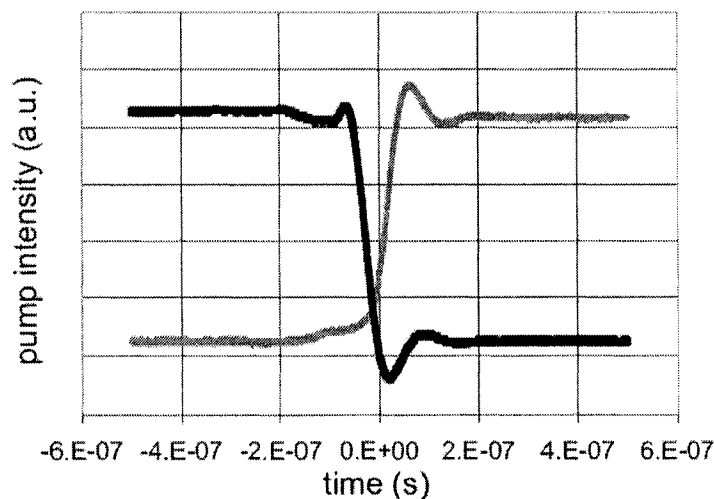


Figure 4.4: Time resolved pump signal rise and fall (488 nm line of the Ar laser) as recorded by a Si diode. Taken by fellow grad student, A. Hryciw.

or 900 nm interference band-pass filter (BPF) to record the Si nanocluster or Nd  ${}^4F_{3/2} \rightarrow {}^4I_{9/2}$  PL respectively. The transitions that could be measured were limited by the sensitivity of the photomultiplier tube (PMT), which ranged from 400 nm to 1000 nm and had a maximum sensitivity near 900 nm. Because the PMT was less sensitive at 1060 nm, and the PL of the Nd  ${}^4F_{3/2} \rightarrow {}^4I_{11/2}$  transition is much weaker than the Nd  ${}^4F_{3/2} \rightarrow {}^4I_{9/2}$  PL, only the SiO PL and Nd  ${}^4F_{3/2} \rightarrow {}^4I_{9/2}$  PL were measured. The time-resolved PL data were analyzed and binned by a photon counter/multiscalar (Becker-Hickel model PMS-400), which consists of a series of discriminators, gates, and counters (Appendix D) with a time resolution of 250 ns.

To align the fibers the collection fiber was initially connected to the USB2877 spectrometer, and the optics were adjusted to maximize the spectrometer signal. The spectrometer was then removed, and the fiber connected to the PMT to record the PL intensity dynamics.

#### 4.2.4 Low temperature measurements

Measurements were taken to record dynamics as a function of temperature. The sample, held by a brass clamp attached to a cold finger, was placed in a chamber

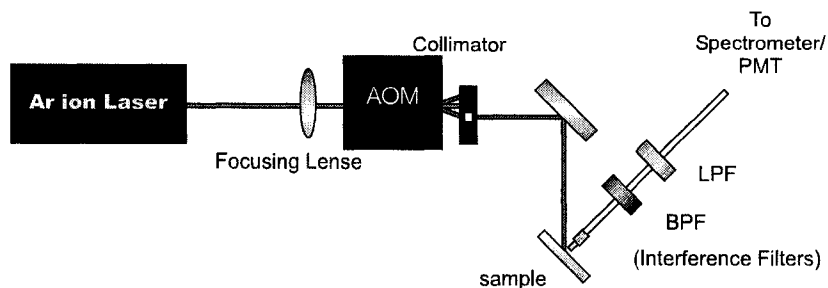


Figure 4.5: Time resolved measurement setup with AOM.

pumped to  $1.8 \times 10^{-6}$  Torr by a turbo pump. The reservoir was filled with liquid nitrogen (77 K) and allowed to equilibrate for half an hour while the temperature was monitored via a thermocouple at the clamp site. If the cryostat was being brought down to 4 K the nitrogen was blown out after equilibration and liquid helium was added. Wavelength and time resolved PL measurements were taken once the cryostat stabilized at the desired temperature.

To obtain PL data the laser beam was directed through a series of focusing and collimating optics to produce a small beam spot ( $< 1$  mm) on the sample within the cryostat at an angle of incidence slightly less than normal. The PL was collected via a set of lenses and focused into an optical fiber. One or more LPFs were used to prevent laser light from entering the fibers (Fig. 4.6), and a BPF was used to isolate a PL band during time resolved measurements.

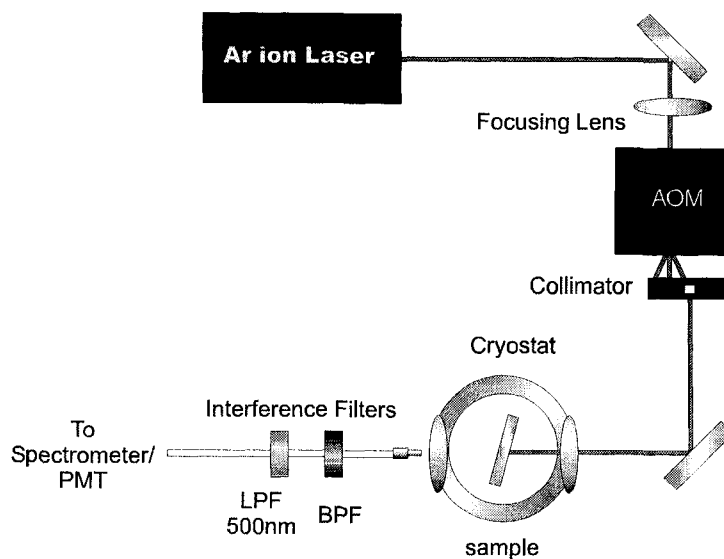


Figure 4.6: Low temperature time resolved setup.

Laser	Wavelength (nm)	Energy (eV)
HeCd	325	3.815
	442	2.805
Ar-ion	454	2.731
	457	2.713
	465	2.666
	472	2.627
	476	2.605
	488	2.541
	496	2.500
	501.7	2.471
514	2.412	

Table 4.2: Laser lines of the HeCd and Ar-ion lasers.

filter type	midpoint (nm)	range (nm)
long pass	550	> 550
band pass	900	850-950
variable band pass	680	650- 715

Table 4.3: Filters used in wavelength- and time-resolved photoluminescence measurements.

# Chapter 5

## Results

### 5.1 Film composition

The initial samples (set A) were made using a  $\text{Nd}_2\text{O}_3$  source and a shielded SiO thermal source to produce a film approximately 100 nm thick. The composition was determined on microprobe by testing 5 points on each sample and averaging the results. The Nd concentration was found by WDS analysis to range from 0.14 to 0.30 atomic % over the six samples, in a matrix of  $\text{SiO}_{1.2}$  (Table 5.1). The higher ratio of oxygen to silicon could be due to penetration of the microprobe beam through the thin film and into the silicon dioxide substrate. The oxygen introduced into the film by co-evaporation of  $\text{Nd}_2\text{O}_3$  would only increase the oxygen content by  $\sim 0.3$  atomic % based on the ratio of oxygen to Nd atoms, less than the  $\sim 5\%$  difference seen here. EDS also indicated the presence of gadolinium in the samples. The Nd film source was therefore also tested and found to contain gadolinium at approximately half the concentration of neodymium, identical to the ratio found to be present in the films (Table 5.1). This was unexpected, since the purchased  $\text{Nd}_2\text{O}_3$  source was nominally 99% pure. Some literature research into the providence of the rare earth elements indicated that Nd and Gd can be difficult to chemically separate. Neodymium is naturally found only as a component of minerals (e.g. xenotime) which contains other RE elements. For the purpose of this study gadolinium is inert as its first excited state is approximately 4 eV above the ground state, which is well above the pump energy used in the PL experiments.

In the second set of samples (set B) a Nd metal source was used to produce

a film  $\approx 200$  nm thick. No Gd was found by EDS in either the metal source or the thin film, however there was a low concentration of aluminum observed (Table 5.1). Aluminium impurities were monitored with the microprobe and found on average to be less than 0.02 atomic %. In this set the Nd concentration ranged from 0.44 to 1.72 atomic % in a matrix of  $\text{SiO}_{1.0}$ , again averaged over 5 points per sample. The difference in the surrounding matrix could have been due to the thicker film, which reduced the penetration of the beam into the  $\text{SiO}_2$  substrate. Microprobe analysis was also done on the Nd doped  $\text{SiO}_2$  reference sample grown under the same conditions as set B; the Nd concentration was 0.26 atomic % in a matrix of  $\text{SiO}_{2.0}$ .

Set B			
Si	O	Nd	Al
49.81	49.71	0.44	0.04
49.79	49.72	0.47	0.01
49.82	49.69	0.49	0.01
49.25	50.15	0.60	0.01
49.51	49.57	0.92	0.00
48.93	49.34	1.72	0.02

Table 5.1: Electron microprobe results of 5 different samples (atomic %). Results are averaged over five points per sample.

The crystal size and structure (amorphous/crystalline) was expected to be the same in the undoped samples as in the doped samples. No effect on the microstructure of the Si clusters was reported in numerous previous studies of Er doped Si nanoclusters for concentrations as low as those used here. At these concentrations,  $3.43 \times 10^{19}$  to  $1.00 \times 10^{20}$  ions  $\text{cm}^{-3}$ , Nd separation is on the order of a few nm. Nd is likely present as isolated ions or possibly small clusters of a few atoms (See Section 2.5) and, therefore, cannot be imaged by TEM.

## 5.2 Si nanocluster PL

Steady-state wavelength-resolved PL of the graduated sample doped with the 0.15 atomic % Nd and annealed at  $400^\circ\text{C}$  (Fig. 5.1) was compared to PL from the undoped sample annealed at  $400^\circ\text{C}$  studied in Ref. [3]. Three PL intensity peaks

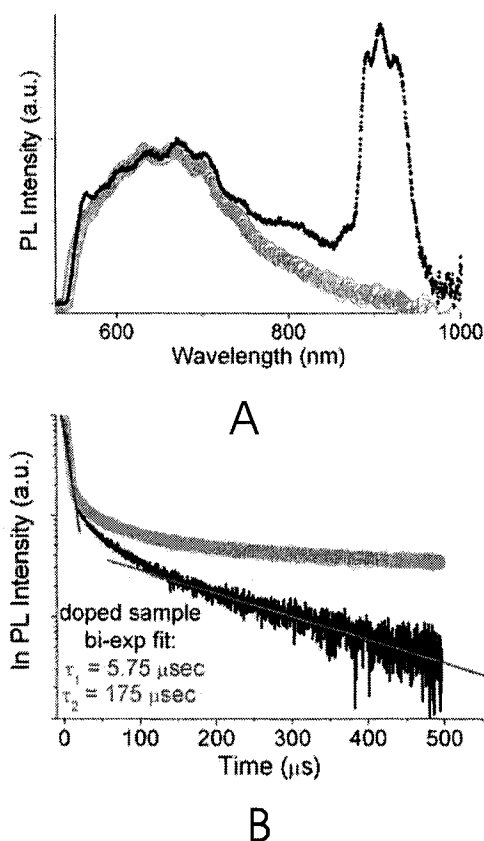


Figure 5.1: PL from specimen set A (0.14 atomic % Nd) (black) and an undoped SiO film (grey), both annealed at 400°C. A) PL spectra from samples used in lifetime measurements. Oscillations in the 600 to 700 nm range are due interference effects of the thin films. (B) Time resolved data for the broad Si nanocluster band.

from the doped sample can be observed in Fig. 5.1: two peaks associated with Nd transitions (the  ${}^4F_{5/2} \rightarrow {}^4I_{9/2}$  Nd transition centred at  $\sim 800$  nm and the  ${}^4F_{3/2} \rightarrow {}^4I_{9/2}$  Nd transition centred at  $\sim 900$  nm), and a broad peak centred at 650 nm. The broad PL intensity peak at 650 nm had a full width at half maximum of 200 nm, as did the broad intensity peak at 650 nm from the undoped sample annealed at 400°C [3] associated with luminescent Si nanoclusters. The broad PL intensity peak in the doped samples will be referred to as the amorphous Si nanocluster PL for the rest of the thesis.

The Si nanocluster PL was also clearly visible in sample set A (with 0.14

atomic % Nd) for annealing temperatures of 400 to 600°C, and 900 to 1100°C (PL was not discernable at 700 or 800°C). Previous work has determined the crystallization temperature of the SiO nanoclusters to lie between 800 and 900°C; at 800°C or lower the clusters are completely amorphous [3]. The change in the PL intensity peak centre and shape with annealing temperature (Fig. 5.3) of the doped samples is similar to that recorded from undoped samples in Ref. [3]. The PL intensity maxima from sample set A and the undoped SiO film [3] were compared for annealing temperatures from 400 to 600°C in Table 5.2. Both Si nanocluster PL maxima shift to longer wavelengths with increasing annealing temperature.

Undoped SiO		
Annealing Temperature (°C)	$\frac{\text{integrated } I_{temp}}{\text{integrated } I_{400}}$	Peak Wavelength (nm)
400	1.00	650
500	0.79	700
600	0.39	730

Nd doped SiO		
Annealing Temperature (°C)	$\frac{\text{integrated } I_{temp}}{\text{integrated } I_{400}}$	Peak Wavelength (nm)
400	1.00	653
500	0.54	690
600	0.19	705

Table 5.2: Comparison of the integrated Si nanocluster PL from the undoped [22] and doped (sample set A) SiO films, normalized to the 400°C anneal.

The decay process of the Si nanocluster PL from the doped samples was compared to the undoped samples (Fig. 5.1). The nanocluster PL was selected by a bandpass filter with a passband from 650 to 715 nm (Table 4.3). The Si nanocluster PL intensity from the 0.14 atomic % Nd doped sample decayed with a fast and a slow component that approximately fit by the bi-exponential

$$\frac{I}{I_0} = e^{-t/\tau_1} + e^{-t/\tau_2}, \quad (5.1)$$

where  $t$  is time, and  $\tau_1$  and  $\tau_2$  are the fast and slow time constants respectively. Only a few points were recorded from the fast decay (Fig. 5.1 B). The fast PL decay has a time constant on the order of a microsecond (the temporal binning of the system was  $0.250 \mu\text{s}$ , therefore only a few points along the decay curve were recorded), while the slower PL decay occurred over a few hundred microseconds. The amorphous nanocluster PL decay curve from the 0.14 atomic % Nd doped sample was fit by a decay lifetimes of  $\tau_1 \sim 5$  and  $\tau_2 \sim 175 \mu\text{s}$  (Fig. 5.1 B, black line).

Strongly multi-exponential PL decays, which include bi-exponential and stretched exponential decays, are characteristic of amorphous silicon nanoclusters [68] and amorphous silicon in general [69]. The Si nanocluster PL dynamics observed from the doped SiO film were similar to those observed in identically processed undoped SiO sample (Fig. 5.1 B). Though the Si nanocluster dynamics were not the focus of this work, the fast decay has been attributed to geminate pair recombination [70], and the slow decay to distant pair recombination [70].

### 5.3 Absorption measurements

Two broad structures were observed in the absorption measurements, one centred at  $\sim 500 \text{ nm}$ , and centred one at  $\sim 850 \text{ nm}$ . These peaks, however, shift with changes in thickness (due to the Nd concentration) in the graduated Nd concentration sample. The nearly  $200 \text{ nm}$  wide structure centred at  $850 \text{ nm}$  was much wider and taller than expected for the  ${}^4I_{9/2} \rightarrow {}^4F_{5/2}$  or  ${}^4I_{9/2} \rightarrow {}^4F_{3/2}$  Nd transitions centred at  $\sim 808 \text{ nm}$  and  $\sim 900 \text{ nm}$  respectively. Neither of these structures were therefore attributed to the amorphous Si nanoclusters or the Nd transitions. They are therefore attributed to film thickness effects.

Interference caused by the substrate-film and film-air interfaces created a substantial oscillation over the entire transmission spectrum. The frequency of the oscillations decreases with increasing thickness. Due to the low Nd concentrations in the thin film and the very low excitation cross-sections, it was impossible to distinguish features due to absorption from the interference.



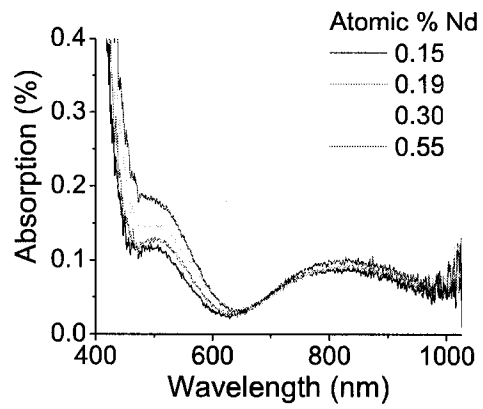


Figure 5.2: Absorption spectra of various concentrations of Nd across the graduated-Nd-concentration sample. The detector limit is 350 nm, according to Ocean Optics specifications.

## 5.4 Nd PL of specimens annealed from 300 to 1100 °C

PL spectra were recorded to determine the effect of annealing temperature on the Nd luminescence (Fig. 5.3). For the rest of this thesis the term “Nd PL” will refer to the luminescence arising from the  ${}^4F_{3/2} \rightarrow {}^4I_{9/2}$  transition unless otherwise specified. The Nd PL was composed of 3 sub-peaks centred at 890, 900, and 925 nm, the ratios of which did not change with annealing temperature. Set A (0.14 atomic % Nd) was annealed from 400°C to 1100°C in 100°C intervals, and both the Nd and Si nanocluster luminescence were detected (Fig. 5.3). The Nd luminescence was most intense when annealed at 500°C, and then decreased with increasing annealing temperature. At annealing temperatures greater than 800°C the Nd luminescence was no longer distinguishable from the Si nanocluster luminescence.

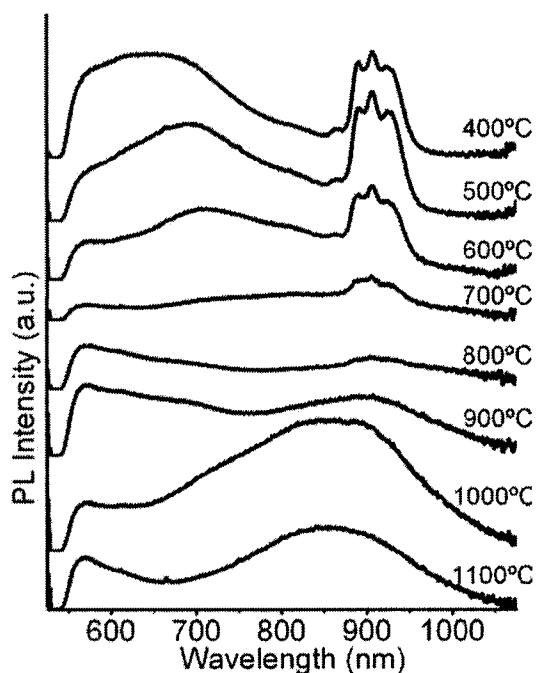


Figure 5.3: Photoluminescence data for Specimen Set A (0.14 atomic % Nd) for various annealing temperatures. The Nd PL at  $\sim 900$  nm decreases with increasing annealing temperatures.

To integrate the Nd luminescence the Si nanocluster luminescence was first subtracted from the data. This was achieved by fitting the nanocluster luminescence to a Gaussian (Fig. 5.4), and then subtracting the calculated fit from the data (Fig. 5.5). The data were then summed from 840 nm to 985 nm.

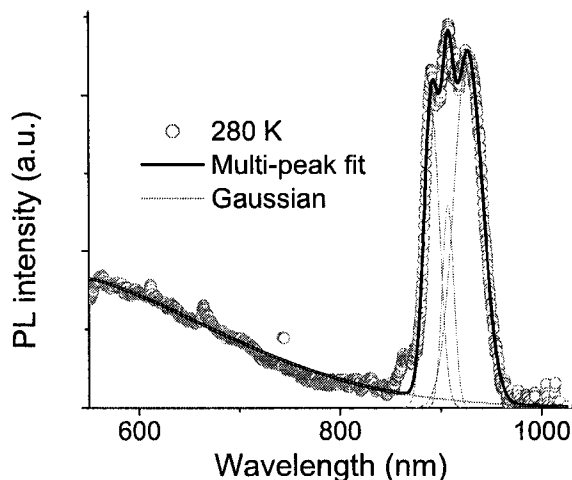
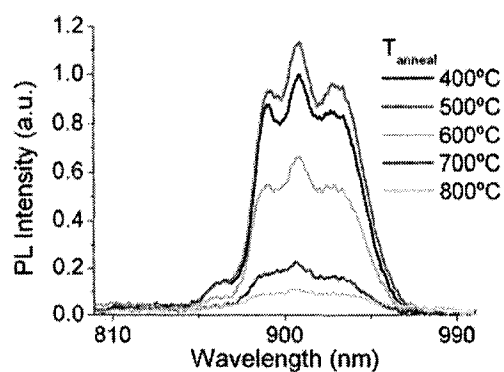
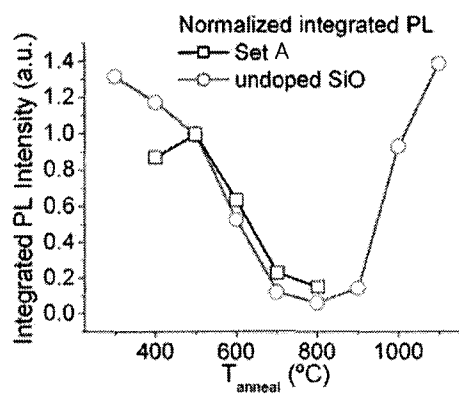


Figure 5.4: Photoluminescence data from a doped (0.14 atomic % Nd) SiO film annealed at 300°C (grey circles) and the fit (black line) to the sum of multiple Gaussian curves (red lines).

The integrated Nd luminescence increased by  $\sim 15\%$  from 400 to 500°C, then decreased by  $\sim 86\%$  from 500 to 800°C. The Nd integrated PL intensity was approximately proportional to the integrated undoped Si nanocluster PL intensity from Ref. [3] for annealing temperatures from 500 to 800°C (Fig. 5.5 B). At annealing temperatures above 800°C the Nd PL was indistinguishable from the Si nanocrystal [3] PL (Fig. 5.3). A similar result for annealing temperatures greater than 800°C (crystallization temperature of the nanoclusters) was previously reported for Nd doped Si nanocrystal films with an overall composition of  $\text{SiO}_{1.0}$  in Ref. [62].



A



B

Figure 5.5: A) Nd PL data from set A, with the Gaussian fit to the nanocluster PL subtracted from the data. B) Integrated luminescence intensity of the Nd PL (set A), and the undoped SiO Si nanocluster PL (undoped SiO plot modified after [3]) .

The effect of annealing temperature  $\text{Nd}^{3+}$  luminescence on higher concentrations of Nd was also studied with set B, doped to 0.44 atomic % Nd. Specimens were annealed at temperatures of 300, 400, and 500°C, to test annealing temperatures near that which produced the maximum observed PL intensity in specimen set A. Three principal Nd luminescence bands were observed from the sample, requiring the use of two spectrometers to cover the full wavelength range. The long-wavelength limit of the visible-to-IR spectrometer detector was 1000 nm, while the short wavelength limit of the IR spectrometer was 900 nm (according to OOI manufacture's specifications). To obtain the PL peak height ratios the data from the two spectrometers were normalized such that the PL intensity in the 900 - 1000 nm range overlapped. The PL peak centred at  $\sim 900$  nm was greater than the peak centred at  $\sim 1060$  nm for all specimens, consistent with previous reports of  $\text{SiO}_2$  samples doped with  $\sim 10^{19}$  Nd ions/cm<sup>3</sup> [21, 71]. The ratio of the integrated luminescence intensity in the three principle Nd luminescence bands remained constant for all three annealing temperatures, but the overall PL intensity was greatest for an annealing temperature of 400°C (the difference in annealing temperatures to produce maximum PL intensity based on Nd concentrations is discussed in Section 6.3). In the work that follows all data were obtained from specimens annealed at 400 C, unless otherwise specified.

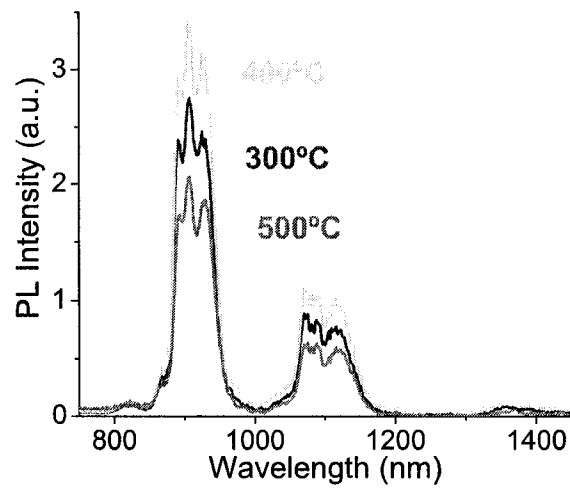


Figure 5.6: Photoluminescence data for Specimen Set B (0.44 atomic % Nd) annealed at 300, 400 and 500°C. Data from two spectrometers are stitched together at approximately 950 nm to display a greater spectral range.

## 5.5 Nd PL of the graduated-Nd-concentration sample

PL data were taken at regular intervals across the graduated Nd composition specimen (see Section 3.3) to investigate the effect of Nd concentration on the luminescence spectrum. The Nd concentration at each point was estimated by electron microprobe analysis. At the lowest Nd concentration the Si nanocluster

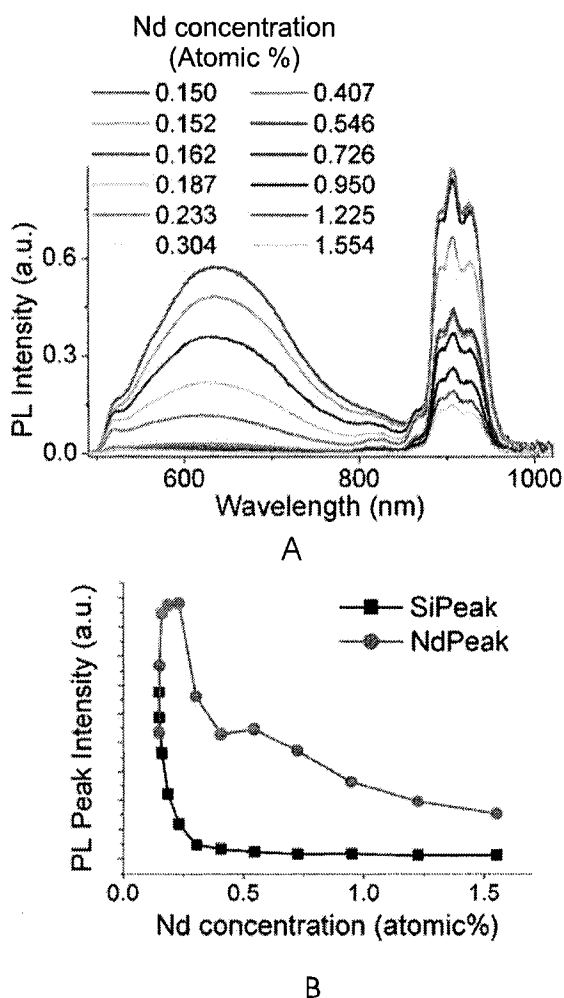


Figure 5.7: A) PL taken at intervals across the graduated sample. B) PL intensity from the Si nanoclusters and Nd ions, integrated from 550 to 800 nm and from 860 to 1000 nm, respectively.

PL intensity was greater than the Nd integrated peak intensity (Fig. 5.7 A and B). The amorphous-Si nanocluster PL intensity decreased as the Nd PL intensity increased to a maximum Nd PL intensity at 0.23 atomic % Nd. For concentrations above 0.23 atomic % Nd the integrated Nd luminescence decreased, while the Si nanocluster luminescence continued to decrease until it was quenched at 0.41 atomic % Nd (Fig. 5.7 B). The decrease in PL with concentration is characteristic of concentration quenching effects (Section 2.5). A similar PL intensity decrease was observed in the samples from set B.

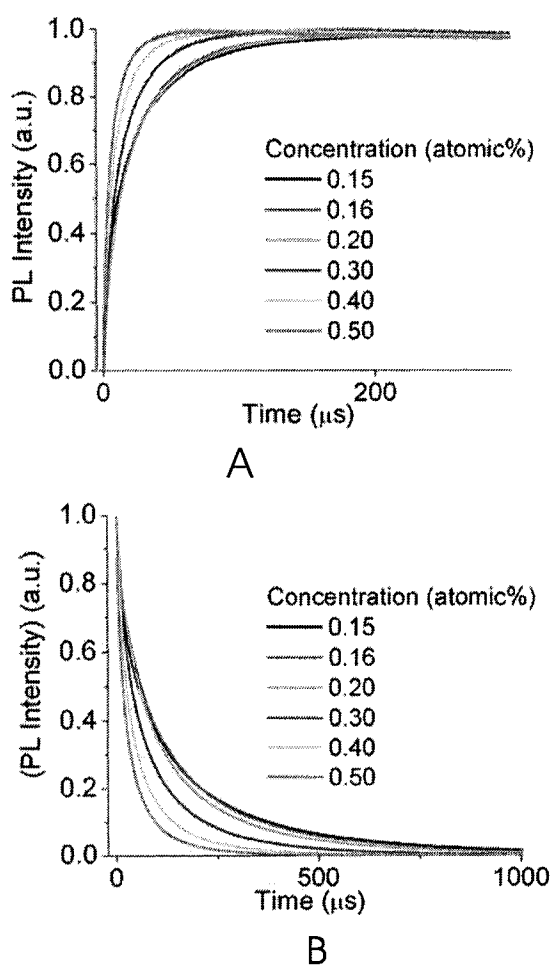


Figure 5.8: Time resolved Nd PL from the graduated Nd concentration sample. A) rise data, B) decay data.



Concentration quenching in the graduated sample was probed further by time resolved measurements of the Nd PL taken at six points (six different concentrations) across the graduated-concentration-sample (Fig. 5.8, Fig. 5.11). The Nd PL decay was plotted on a logarithmic scale (Fig. 5.9, B). The resulting curve resembled a power law, indicative of a stretched exponential decay:

$$\frac{I_d}{I_0} = \exp\left(-\left(\frac{t}{\tau_d}\right)^{\beta_d}\right), \quad (5.2)$$

where  $I_d$  is the PL intensity at time  $t$ ,  $I_0$  is the initial intensity,  $\tau_d$  is the  $1/e$  decay time, and  $\beta_d$  is between 0 and 1 ( $\beta=1$  is a single exponential). Eq. 6.4 was fitted to the data by varying  $\tau$  and  $\beta$ , and was plotted as  $\log(-\ln(I_d/I_0))$  vs.  $\log(t)$  to obtain the time constant,  $\tau_d$ , from a linear fit (Fig. 5.10 B). The resultant linear fits (slope =  $\beta$ , intercept =  $-\beta \log \tau$ ) produced an average  $R^2$  of greater than 0.999, indicating a better fit than to a single exponential ( $R^2 < 0.9$ ), or a bi-exponential ( $R^2 < 0.99$ ). It is noted that a bi-exponential can be fit by a stretched exponential if the bi-exponential is noisy.

The time constant  $\tau_d$  was constant within error at  $\sim 25 \mu\text{s}$  for concentrations less than 0.3 atomic % (Fig. 5.11). At concentrations of 0.3 atomic % and greater  $\tau_d$  decreased monotonically to  $\approx 7 \mu\text{s}$  at 0.5 atomic %. An increasing PL decay rate with increasing Nd concentration is generally indicative of concentration effects dominating the decay dynamics of the Nd ions [20, 21]. Quenching effects dominate after a threshold concentration [20, 21, 9], here at approximately 0.3 atomic % Nd, similar to the 0.2 atomic % Er concentration with amorphous nanoclusters from reference [33].

The rise of the Nd PL intensity was also fit by a stretched exponential,

$$\frac{I_r}{I_0} = 1 - \exp\left(-\left(\frac{t}{\tau_r}\right)^{\beta_r}\right), \quad (5.3)$$

where  $I_r$  is the PL intensity,  $\tau_r$  is the  $1/e$  rise time, and  $\beta_r$  varies from 0 to 1 (as for  $\beta_d$ ). When plotted as  $\log(-\ln(1 - I_r/I_0))$  versus  $\log(t)$  (slope =  $\beta$ , intercept =  $-\beta \log \tau$  as in the previous case) the Nd PL data could be fit by a straight line. The rise times were constant within error at approximately  $20 \mu\text{s}$  for concentrations above 0.3 atomic % Nd, and decreased to approximately  $10 \mu\text{s}$  at 0.5 atomic %

Nd. Results for the stretched exponential fits of the time resolved Nd PL are shown in Figs. 5.11 and 5.12.

Concentration (atomic %)	$\tau_r$ ( $\mu\text{s}$ )	$\beta_r$	$R^2$	$\tau_d$ ( $\mu\text{s}$ )	$\beta_d$	$R^2$
0.15	19.0	0.605	0.9996	24.1	0.605	0.9996
0.16	20.1	0.696	0.9998	25.9	0.648	0.9995
0.20	21.3	0.711	0.9990	22.9	0.641	0.9975
0.3	14.9	0.760	0.9962	15.9	0.716	0.9993
0.4	9.7	0.725	0.9970	10.4	0.715	0.9978
0.5	7.1	0.753	0.9966	6.7	0.664	0.9992

Table 5.3:  $\tau$  and  $\beta$  from fits to linearized data over various concentrations.

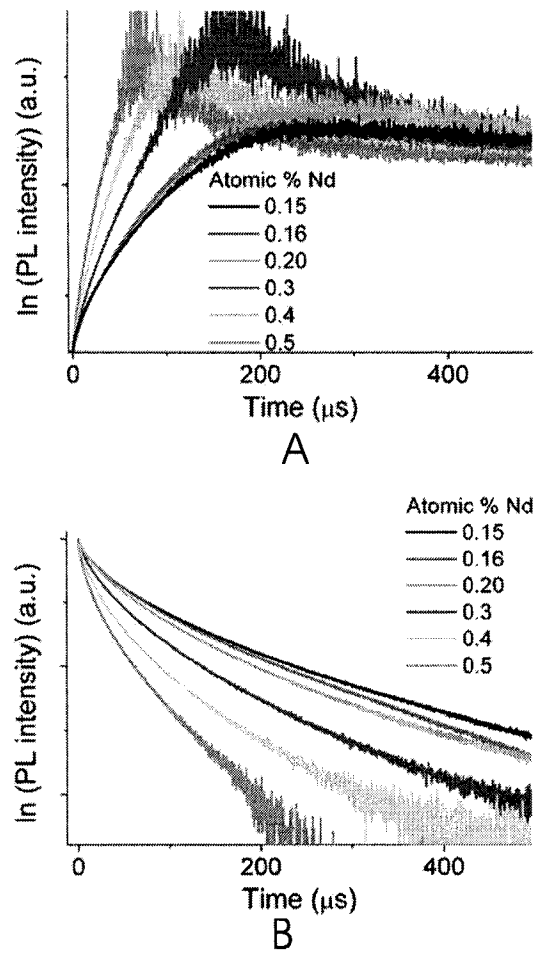


Figure 5.9: Time resolved Nd PL from the graduated Nd concentration sample. A) rise, B) decay.

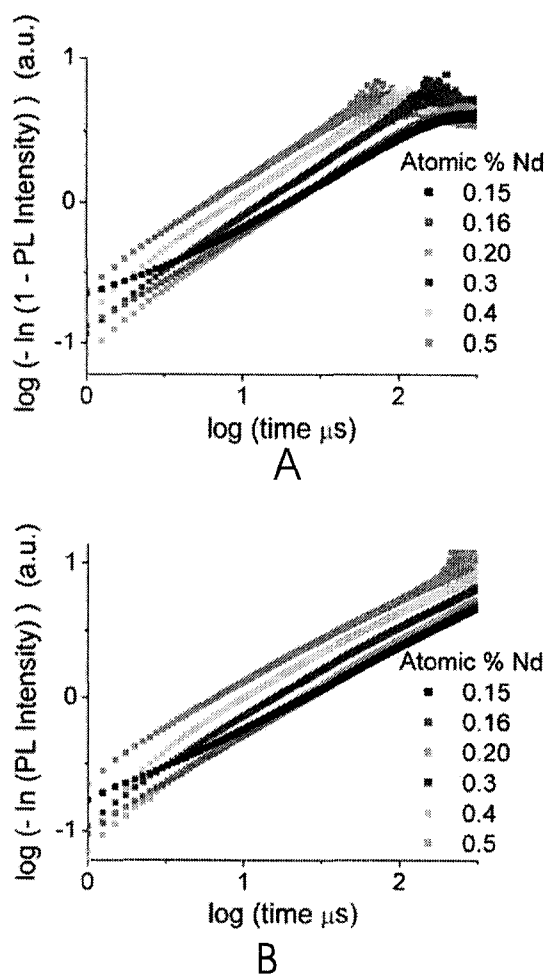
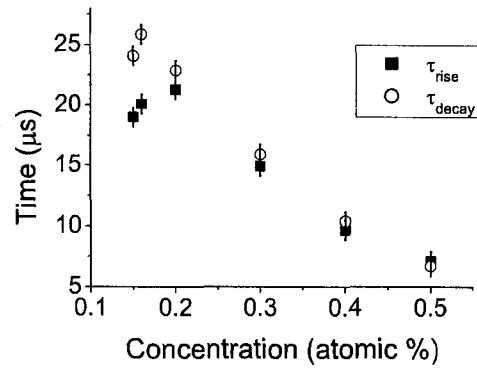
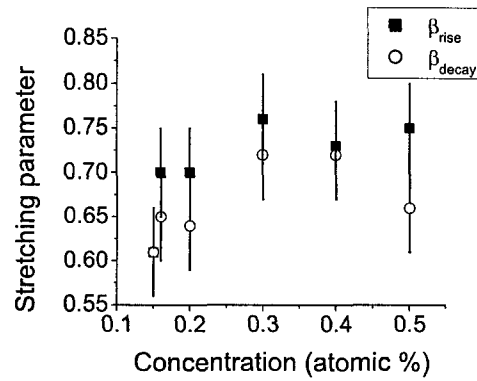


Figure 5.10: Time resolved Nd PL (normalized) of the graduated-Nd-concentration sample. A) rise, B) decay.

Figure 5.11:  $\tau$  from fits to linearized data over various concentrationsFigure 5.12:  $\beta$  from fits to linearized data over various concentrations

## 5.6 Nd PL for various pump energies and powers

PL data were taken from the 0.44 atomic % Nd sample (set B) to determine the effect of pump photon energy on the Nd PL intensity and line-shape, and to determine if the available laser lines were resonant with any of the electronic transitions of Nd. The Ar-ion laser lines (Table 4.2) at 100 mW (as measured by an internal power meter calibrated for each wavelength) excited the sample (Fig. 5.13). The integrated Nd PL intensity increased monotonically with pump energy by a factor of three from 514 to 454 nm. A similar gradual increase in integrated PL intensity as a function of excitation energy was reported in Ref. [62] in a study of Nd doped nanocrystals.

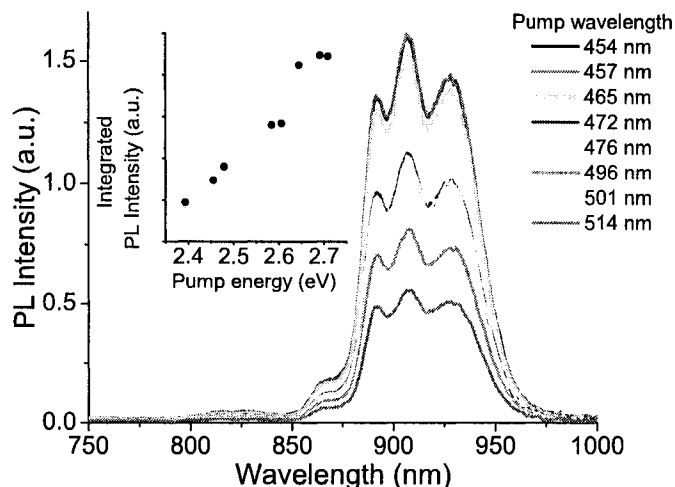


Figure 5.13: Nd PL (0.44 atomic % Nd). Inset shows the integrated PL intensity as a function of excitation energy.

The PL intensity as a function of pump power (i.e., photon flux) was also studied from this sample to determine the power above which pump-rate dependent non-radiative effects dominate (e.g. ‘double excitation’ and co-operative up-conversion - see Section 2.5) The 476 nm line of the Ar-ion laser was used at powers from 60 mW to 2 W. The integrated Nd PL intensity increase was approximately linear up to approximately 250 mW ( $\sim 5 \times 10^{20} \text{ cm}^{-2}$ ), after which the PL intensity began to saturate as the number of excited nanocluster (and, therefore, excited

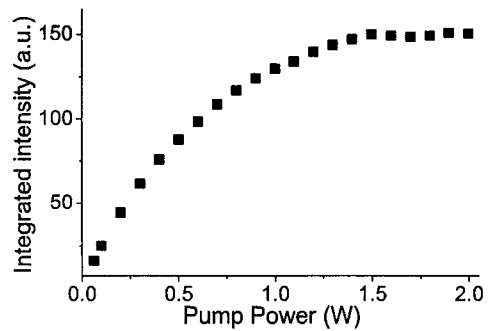


Figure 5.14: Integrated Nd PL intensity as a function of pump power at 476 nm (0.44 atomic % Nd).

Nd ions) reaches a maximum. The sample temperature was allowed to stabilize by taking PL measurements after the sample was allowed to equilibrate for 2 minutes under continuous pumping.

## 5.7 Nd PL at low temperature

An approximately  $1.5 \times 1.5$  cm<sup>2</sup> section of the graduated sample was used in low temperature measurements. The integrated Nd PL intensity data of the graduated concentration sample were fit by an arbitrary polynomial as a function of concentration to estimate the Nd concentration at locations between known points measured by electron microprobe. The Nd concentration of the sample used in the low-temperature experiment was estimated to be  $\sim 0.2$  atomic %.

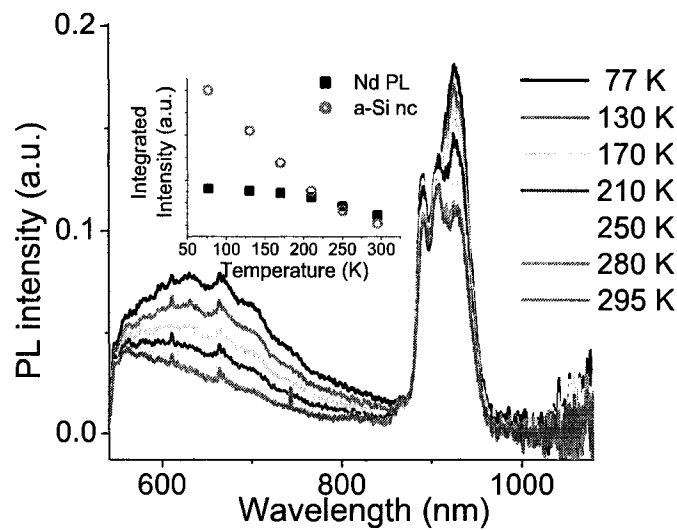


Figure 5.15: PL temperature dependence of the 0.2 atomic % Nd sample. Inset shows integrated PL intensities of Si and Nd PL as a function temperatures.

As the temperature decreased both the Nd PL intensity and Si nanocluster PL intensity increased (Fig. 5.15). When cooled to 77 K, the integrated Nd PL intensity increased to 1.4 times that at 295 K and the integrated Si nanocluster PL intensity increased to 2.8 times that observed at 295 K (Fig. 5.15, inset). To further investigate the change in peak ratios the PL was fit by multiple Gaussian curves as in Section 5.4 (Fig. 5.4), and the heights and peak centres were reported from the fits. Three sub-peaks were resolved in the Nd PL at 890, 900, and 925 nm (Fig. 5.16 A). The intensity peak height of the sub-peak centred at 925 nm (as determined by a Gaussian fit) was the most temperature sensitive (40% increase



from room temperature to 77 K) while the sub-peaks centred at 890 and 900 nm had approximately constant heights (Fig. 5.16 B).

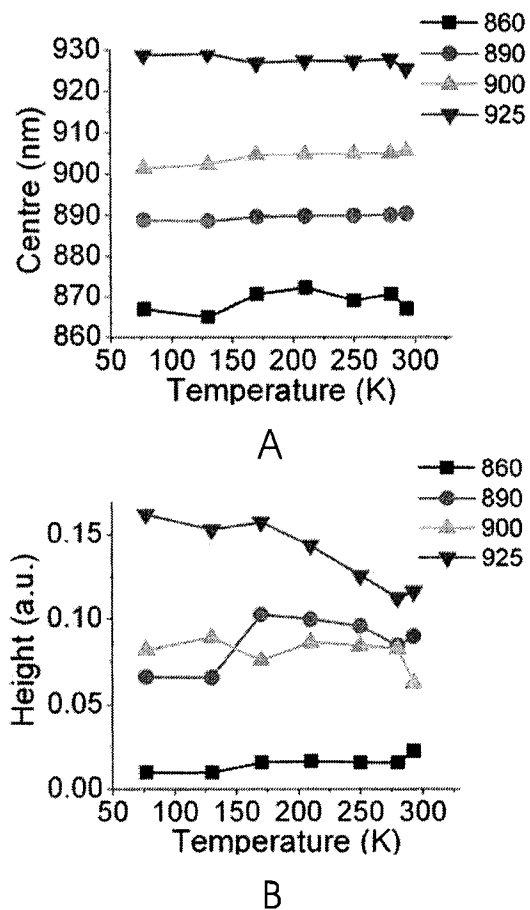


Figure 5.16: Temperature dependence of the Nd PL sub-peaks, fit by Gaussians. A) peak centre, B) peak intensity.

The time resolved Nd PL rise and decay were fit ( $R^2$  greater than 0.999) by a stretched exponential (Eq. 6.3 and 6.4) (Fig. 5.17). The lifetime increased slightly (from 26 to 28  $\mu\text{s}$ ) on cooling from 295 to  $\sim 4$  K suggesting a possible weak temperature dependence (Table 5.4). A similarly weak temperature dependence of the Nd PL was reported in Ref. [62] for a Nd Si nanocrystal film (overall composition of  $\text{SiO}_{1.7}$ ). Although there was little temperature dependence of the lifetime, the PL intensity was reported in [62] to decrease by 80 % and the lifetime to decrease by 20 % on heating from 25 K to room temperature.

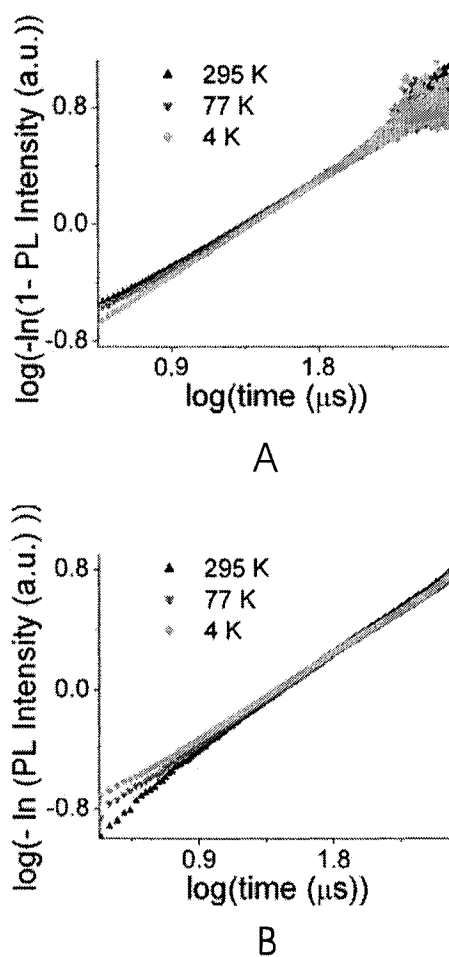


Figure 5.17: Time resolved Nd PL ( $\sim 0.2$  atomic % Nd) at 4, 77, 293 K. A) rise, B) decay.

Temperature K	$\tau_d$ $\mu\text{s}$ ( $\pm 0.5$ )	$\beta$ ( $\pm 0.1$ )	$R^2$	$\tau_r$ $\mu\text{s}$ ( $\pm 0.5$ )	$\beta$ ( $\pm 0.1$ )	$R^2$
4	27.5	0.65	0.9983	28.9	0.75	0.9998
31	28.8	0.67	0.9998	29.0	0.75	0.9996
49	29.6	0.68	0.9998	28.7	0.74	0.9997
65	27.5	0.64	0.9999	28.8	0.74	0.9997
77	26.5	0.64	0.9998	27.6	0.74	0.9989
293	25.8	0.66	0.9998	28.0	0.76	0.9989

Table 5.4: Nd PL time constants ( $\tau$ ) for rise and decay,  $\beta$ , and goodness of fit ( $R^2$  is the coefficient of determination of a linear regression).

## 5.8 Nd PL from Nd-doped SiO<sub>2</sub> thin film

Measurements were taken from a Nd-doped SiO<sub>2</sub> sample prepared under identical conditions as the other samples (using a SiO<sub>2</sub> source instead of SiO). Nd PL was observed in the Nd-doped SiO film when illuminated with the 476 nm laser line, however none was observed from the Nd-doped SiO<sub>2</sub> film though the pump power was increased by two orders of magnitude and the collection time increased by three orders of magnitude.

## 5.9 Nd PL from Nd-doped silica laser glass

PL measurements were taken from a Nd doped silica laser glass produced by Keiger Incorporated to compare the results to those from the nanocluster specimens. Typical for laser glasses, aluminum and other impurities are incorporated in the glass to reduce Nd clustering so that higher Nd concentrations may be used. The Nd absorption spectra is non-zero over the range of Ar-ion laser wavelengths due to the inhomogeneous broadening caused by the Nd environment [72], therefore the laser glass could be excited with 476 nm Ar-ion laser line.

PL intensity peaks centred at 808, 880, 1062, and 1330 nm (Fig. 5.19) were identified from the laser glass, necessitating the use of two spectrometers which were normalized as discussed in Section 5.4. The peaks in both the SiO and silica samples were fit by multiple Gaussians (structure within a single PL band is referred to as sub-peaks) (Fig. 5.18). The Nd PL intensity peaks observed from the silica laser glass were at similar wavelengths as those seen amorphous-Si-nanocluster host (Fig. 5.19, Table 5.5). All PL bands are much narrower than those found in the Nd-doped SiO films, and ratios of the sub-peaks were also different (Table 5.5).

Time resolved Nd PL from the laser glass sample was compared to the Nd PL of the nanocomposite sample. The Nd PL intensity rise and decay data were fit by stretched exponentials (Eq. 6.3, 6.4), as in the Nd doped Si nanocomposite case. The stretching parameter,  $\beta$ , was found to be approximately unity (0.90 and 0.97 for the rise and decay respectively), indicating the PL rise and decay were effectively single exponentials. A single exponential with noise can, in fact, be

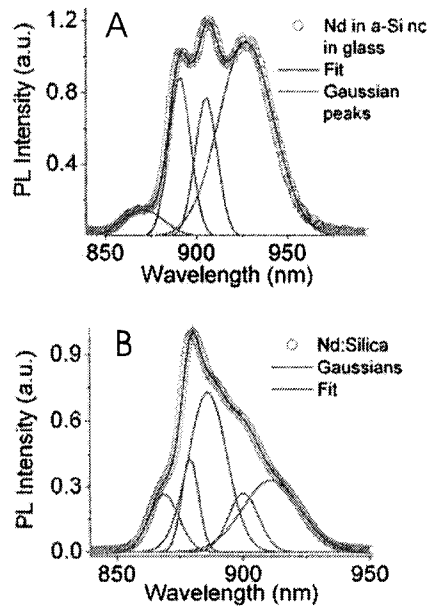


Figure 5.18: Nd PL data and Gaussian fits to A) Nd in the nanocluster films (denoted as Nd in a-Si nc), and B) Nd in silica laser glass.

better fit with a stretched exponential with a high  $\beta$ . The Nd PL rise and decay time,  $\tau_r$  and  $\tau_d$ , of the laser glass were 366 and 335  $\mu\text{s}$  respectively (Fig. 5.20), more than an order of magnitude longer than those of the nanocluster sample ( $\sim 28$  and 25  $\mu\text{s}$  respectively).

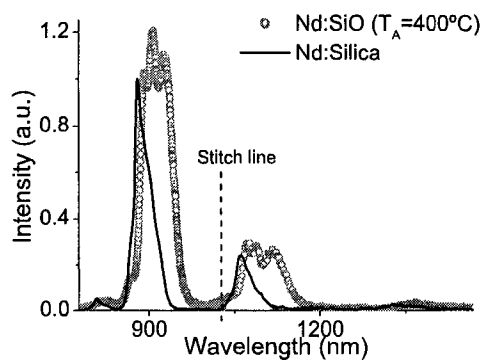


Figure 5.19: Nd PL spectra from doped silica laser glass (black line) and Nd doped (0.44 atomic % Nd) amorphous Si nanocluster glass (grey circles). The stitch line indicates where data from two spectrometers were joined.

Nd Transition	Nd sub-peaks from specimen B (0.44 atomic % Nd)		Nd sub-peaks from Nd laser glass	
	Wavelength nm	Height a.u.	Wavelength nm	Height a.u.
${}^4F_{5/2} \rightarrow {}^4I_{9/2}$	822	0.0388	812	0.0382
${}^4F_{3/2} \rightarrow {}^4I_{9/2}$	870	0.142	870	0.309
	891	0.912	879	0.497
	905	0.770	886	0.6722
	927	1.083	898	0.379
			912	0.3207
${}^4F_{3/2} \rightarrow {}^4I_{11/2}$	1075	0.246	1061	0.136
	1121	0.238	1072	0.120
${}^4F_{3/2} \rightarrow {}^4I_{13/2}$	1374	0.023	1335	0.0163

Table 5.5: Peak wavelengths and heights from Gaussian fits.

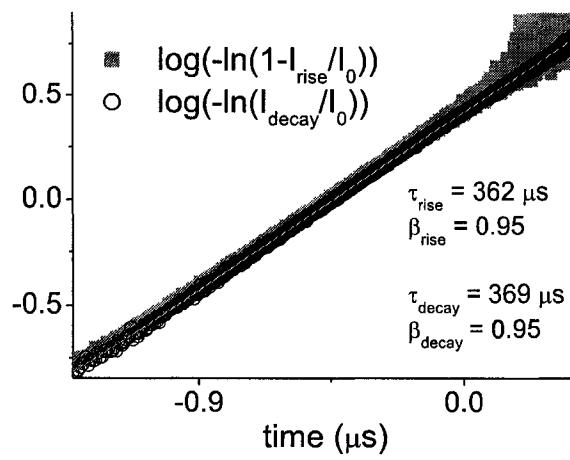


Figure 5.20: Time resolved Nd PL of the Nd laser glass. Lines are fits to the data.

# Chapter 6

## Discussion

### 6.1 Comparison of nanocluster PL in doped and undoped specimens

The presence of Nd was not expected to affect nanocluster nucleation and growth at the low concentrations used in this study ( $\sim 9 \times 10^{19} \text{ cm}^{-3}$ ). There are several indirect lines of evidence to suggest that the microstructure of the clusters was indeed similar to the undoped SiO samples. The broad PL peak observed from the specimen doped with 0.14 atomic % Nd and from the undoped SiO specimen had the same peak wavelength and full-width at half-maximum when annealed at 400°. As the annealing temperature increased the broad peaks of both samples shifted to longer wavelengths in roughly the same increments (Fig. 5.3, Table 5.2). Based on this identical spectra shift with increasing annealing temperature, the nucleation and growth of nanoclusters were apparently unaffected by the presence of Nd. The PL decay from both specimens displayed bi-exponential behaviour with a fast (on the order of a  $\mu\text{s}$ ) and slow (on the order of a few hundred  $\mu\text{s}$ ) component (Fig. 5.1 B). The source of the broad PL peak was therefore attributed to amorphous Si nanoclusters with radii on the order of a few nm, similar to those discussed in Ref. [3].



## 6.2 Estimate of Nd environment based on PL

The Nd PL from the nanocluster specimens was compared to PL from Nd in a Si nanocrystal film [62], in hydrogenated bulk amorphous silicon [4], in porous silicon [5], and in silicon-based gels [6]. The Nd PL intensity from each of the hosts displayed peaks from the major transitions ( ${}^4F_{3/2} \rightarrow {}^4I_{9/2}$ ,  ${}^4F_{3/2} \rightarrow {}^4I_{11/2}$ , and  ${}^4F_{3/2} \rightarrow {}^4I_{13/2}$ ) at slightly different peak wavelengths (Fig. 6.1). The ratio of the intensity sub-peaks making up the PL intensity peaks (as fit by multiple Gaussian curves) was also host dependent. These differences in PL intensity peak wavelengths were due to the Nd environment; for example, in the laser glass the dopants used to maximize the lifetime have been reported to blue shift the PL by 20 nm [73]. Comparing the spectra of the Nd PL from the nanocluster specimen to the Nd PL reported by [4], [5], and [6] suggested that the PL of the nanocluster sample was due to a combination of Nd in  $\text{SiO}_2$  and Nd in amorphous Si.

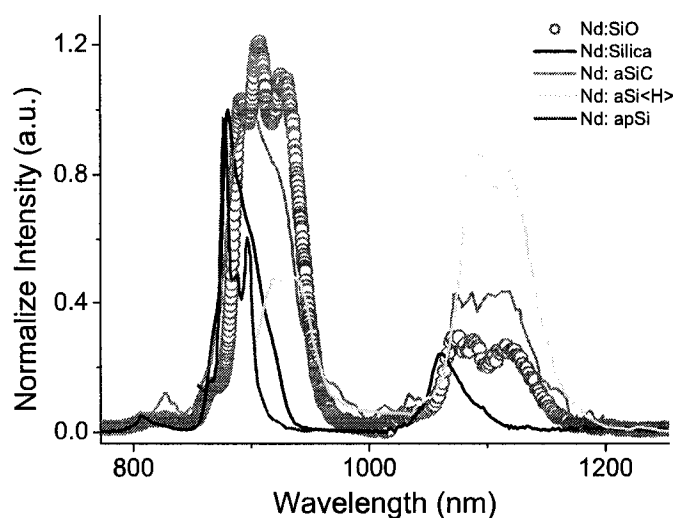


Figure 6.1: Nd PL from  $\text{SiO}$  doped with 0.44 atomic % Nd (Nd:SiO). Plots of normalized Nd PL from Nd doped silica (Nd:Silica), amorphous bulk silicon containing carbon (Nd:aSiC), bulk amorphous hydrogenated silicon (Nd:aSi<H>), and amorphous porous silicon (Nd:apSi), modified after [4], [5], and [6] are shown on the same axis.

The Nd PL intensity from the laser glass had a decay time more than an or-

der of magnitude longer than that of the Nd PL from the nanocluster sample. Laser glass is designed to have an extended lifetime (for example, through doping to reducing RE clustering). The Nd concentrations used in the nanocluster films ( $\sim 9 \times 10^{19} \text{ cm}^{-3}$  Nd) are above threshold concentration for clustering in silica glass ( $\sim 10^{19} \text{ cm}^{-3}$  [21]). Though it has been reported that Nd is slightly more soluble in sub-stoichiometric silicon oxide than in pure silica [6], Nd clustering is a possible explanation for the shorter lifetimes observed in the amorphous nanocluster specimens compared to the laser glass (discussed in Section 6.4). These may not be metallic Nd clusters (nearest-neighbours are Nd), but simply local high-Nd environments (nearest-neighbours are Si or O, but the separation between  $\text{Nd}^{3+}$  ions is only several atoms) in which the cross-relaxation and excitation migration processes discussed in Section 2.5 can dominate.

### 6.3 Effect of annealing temperature on Nd PL

The integrated Nd PL intensity of the 0.14 atomic % Nd sample initially increased from 400 to 500°C, then decreased as the annealing temperature increased from 500 to 800°C similar to the decrease observed from undoped Si-nc integrated PL intensity (Fig. 5.5). The average size of the nanoclusters changed with thermal processing, affecting the nanocluster energy levels and bandtails [39, 55]. Higher temperatures also activate ion migration, increasing the chance of Nd clustering (discussed in Section 6.5). The overall decrease in Nd PL intensity with increasing annealing temperature could be due to changes in the nanocluster size (back-transfer effects and non-radiative transitions on the nanoclusters), Nd concentration effects (clustering), or a combination of the two.

As previously discussed (Section 2.5), the probability of a PL-reducing transfer from the excited ion back to a nanocluster is greater for small energy differences between the ion and nanocluster excited states. The nanocluster PL shifted to longer wavelengths as the annealing temperature increased, approaching the Nd PL peak resulting from the  ${}^4F_{3/2}$ -to-ground state transition. Back-transfer effects may have become more dominant, thus reducing the Nd PL, because the energy levels were more closely matched at higher annealing temperature.

Non-radiative transitions occurring on the nanoclusters produced at higher

temperatures would reduce the Nd PL if the non-radiative decay rate intrinsic to the nanoclusters was greater than the nanocluster-to-Nd transfer rate. These transitions would also cause a reduction in nanocluster PL, which was observed in these specimens. The band tail energy spread decreases with annealing temperature as the nanoclusters grow and quantum confinement effects are reduced [55]. This may increase the number of carriers from the bandtail states thermally excited to the conduction band [55]. From the conduction band they may then be captured by non-radiative recombination centres (due to dangling bonds and structural disorder [55, 39]), resulting in a net loss of PL from both the clusters and the Nd ions. This established effect could compete with the energy transfer to the  $\text{Nd}^{3+}$  ion, thereby lowering the Nd PL intensity for larger amorphous Si clusters [55].

Increased Nd clustering would lead to a decrease in Nd PL (see Section 2.5), an effect that would be more pronounced at higher Nd concentrations. The Nd PL intensity from the 0.14 atomic % Nd specimen peaked at 500°C (Fig. 5.5), while that from the 0.44 atomic % Nd specimen peaked at 400°C (Fig. 5.6), supporting the postulate that the Nd PL reduction with increasing annealing temperature was linked to Nd concentration effects. The difference in the optimum annealing temperature for sets A and B may have been due to the combined effects of diffusion and Nd concentration. Nd is more soluble in  $\text{SiO}_x$  than in Si [21, 6], and the volume of  $\text{SiO}_x$  (where  $x$  is between 1 and 2) that the Nd ions occupied diminished as the nanoclusters accrued Si. Therefore, though the Nd concentration in the total film was  $9 \times 10^{19} \text{ cm}^{-3}$ , the concentration of Nd in  $\text{SiO}_x$  approached  $2 \times 10^{20} \text{ cm}^{-3}$  as more Si precipitated and  $x$  approached 2. The concentration threshold for concentration quenching in  $\text{SiO}_2$  is  $\sim 10^{19} \text{ cm}^{-3}$  in silica glass [6], therefore it is possible that the phase separation of SiO forced Nd into a smaller volume where the effective concentration was such that they would cluster, reducing Nd PL.

## 6.4 Effect of Nd concentration on Nd PL

The PL intensity in the graduated-Nd-concentration sample increased with increasing concentration up to a threshold concentration ( $\approx 1.5 \times 10^{20} \text{ ions cm}^{-3}$ ), then decreased monotonically with concentration (Fig. 5.7). If the PL intensity

was limited only by the nanoclusters available to excite the Nd ions, the intensity would be expected to plateau once the Si nanocluster PL was undetectable. The Nd PL decay was constant, within noise, for concentrations from 0.15 to 0.20 atomic %. Above 0.3 atomic % the shape of the decay changed ( $\beta$  increased) while the lifetime decreased rapidly (Fig. 5.8). The decrease in PL intensity and decay time with increasing Nd concentrations suggested that after the concentration increased to 0.3 atomic % Nd new channels opened for the ions to decay non-radiatively. As the separation between ions decreased with increasing concentration, more non-radiative decay channels become available through Nd-Nd interactions (evident as an increased decay rate). The commonly discussed mechanisms are ion clustering [64], excitation migration [21], and co-operative up-conversion [9, 20] (see Section 2.5). Introducing these competing  ${}^4F_{3/2}$  level depopulating processes will result in a net increase in the PL decay rate when the Nd-Nd interaction rates are greater than, or comparable to, the radiative decay rates. This was reflected in the increase of the Nd PL rise and decay rates at higher Nd concentrations (Fig. 5.11).

## 6.5 Nd-to-nanocluster transfer processes

The probability of energy transfer from an excited Nd ion back to a nanocluster (e.g. back transfer and impurity Auger effects) depends on the number of phonons available with enough energy to overcome the energy mismatch between the ion and cluster [50, 61] (see Section 2.5), and therefore will be suppressed at low temperatures. The integrated Nd PL intensity from the  $\approx 0.2$  atomic % Nd specimen decreased by less than 30 % from 4 to 293 K (Fig. 5.15). The PL dynamics also varied only slightly with temperature:  $\beta$  for the rise ( $\sim 0.75$ ) and decay ( $\sim 0.65$ ) were constant, while the rise and decay times decreased from 4 to 293 K by approximately 3 and 11 % respectively. The nearly constant lifetimes as a function of temperature suggested that back-transfer effects were relatively minor. The overall Nd PL temperature dependence of the sample was weak, suggesting that back transfer and impurity Auger effects were weak compared to other non-radiative processes that were occurring (such as concentration quenching effects).

## 6.6 Functional form of Nd radiative decay

Nd PL decays from all the specimens were fit by stretched exponentials, which are often observed in disordered systems [68, 74, 75, 76]. The stretched exponential behaviour was likely due to a combination of Nd energy migration [77, 76], and a distribution of intrinsic Nd PL decay rates [74]. Excitation migration from Nd to Nd ion (see Section 2.5), which is known to occur in Nd doped glasses, has been documented to cause stretched exponential behaviour [77, 76]. The dipolar energy transfer rate varies inversely with Nd separation to the sixth power, and is, therefore, a distribution of rates due to the random arrangement of Nd ions. This results in a distribution of PL decay rates due to migration alone (i.e. assuming identical intrinsic PL lifetimes for all Nd) and produces a stretched exponential PL decay [78], where  $\beta$  would be an indication of the number of intermediate transport Nd ions during migration [76].

The stretched exponential behaviour may also be the result of variations in intrinsic Nd PL decay times induced by structural disorder in the specimen [76] (e.g. varying composition of  $\text{SiO}_x$ , proximity to a Si nanocluster and other Nd ions). Each Nd would decay at a slightly different rate, and this distribution of the rates would result in a stretched exponential decay function [74]. In these specimens the decay was observed to approach a single exponential decay ( $\beta \rightarrow 1$ ) with increasing concentration. This may be due to an increased number of quenching sites introduced by concentration effects, which would potentially limit the number intermediate Nd ions (transport sites) and limit the distribution of relaxation times.

## 6.7 Nd excitation cross-section

The Nd ion can be approximated as a two-level system of  ${}^4I_{9/2}$  (model level 1) and  ${}^4F_{3/2}$  (model level 2) for low Nd concentrations. Non-radiative decay processes are assumed to be minimal because Nd-Nd interactions are weak in the low concentration samples, and the weak temperature dependence of the PL lifetime suggests back-transfer and Auger-related interactions are minimal. The closely spaced Nd energy levels populated by energy transfer should phonon-decay quickly into the  ${}^4F_{3/2}$  level. The transition to the  ${}^4I_{9/2}$  ground state was stronger than transi-

tions to the  ${}^4I_{11/2}$  or  ${}^4I_{13/2}$  levels (based on PL peak intensity ratios), therefore transitions other than to the ground state are ignored.

In a simple two-level system the rate equation at low pump rates is

$$\frac{dN_2}{dt} = RN_2 + w_d N_2, \quad (6.1)$$

where  $N_2$  is the population of the excited state,  $R$  is the excitation rate, and  $w_d$  is the decay rate of the excited state. At low pump flux, where the PL intensity was proportional to flux, the excitation rate is

$$R = \sigma_{eff}^{Nd^{3+}} \times \Phi_{phot}, \quad (6.2)$$

where  $\Phi_{phot}$  is the excitation photon flux (pump power  $\div (hc/\lambda) \div$  area  $\sim 10^{18}$  cm $^{-2}$ s $^{-1}$ ). The population of the excited state after the pump is turned on at  $t = 0$  rises exponentially,  $N_2(t) = 1 - e^{-(R+w_d)t}$ , while the population after the pump is turned off ( $R = 0$ ) at  $t = 0$  decays exponentially,  $N_2(t) = e^{-(w_d)t}$ .

The intensity is proportional to  $N_2$ , and is written as

$$\frac{I_{rise}}{I_0} = 1 - e^{-w_r t}, \quad (6.3)$$

and

$$\frac{I_{decay}}{I_0} = e^{-w_d t}, \quad (6.4)$$

where  $I_0$  is the maximum PL intensity, and  $w_r$  is the measured PL intensity rise rate. The PL measurements always necessarily include the radiative decay, therefore  $w_r$  is a combination of the pump rate to the upper level and the decay rate to the lower one. The PL intensity rise rate is  $w_r = R + w_d$ : as the pump rate increases  $w_r$  must increase, and as  $R \rightarrow 0$   $w_r \rightarrow w_d$ . The effective cross-section can, therefore, be estimated with Eq. 6.2 by fitting Eq. 6.4 and Eq. 6.3 to the decay and rise data respectively, and solving for  $R$ .

The cross-section was estimated without considering the stretching parameter,  $\beta$ , as has been frequently been done in the literature. To the best of my knowledge  $\beta$  has not been incorporated into these calculations previously. Therefore  $\sigma_{eff}^{Nd^{3+}}$  is an *effective* cross-section.

Concentration (atomic %)	Temperature K	$R$ (s <sup>-1</sup> )	$\sigma_{eff}^{Nd^{3+}}$ (10 <sup>-15</sup> cm <sup>2</sup> )
0.15	293	10965	2.8
0.16	293	11171	2.8
0.20	293	3094	0.8
0.3	293	4158	1.0
0.4	293	6995	1.7
0.4	4	4493	1.1
0.4	77	6660	1.7
0.4	293	5332	1.3

Table 6.1: Effective excitation cross-sections for low concentrations of Nd in SiO.

The direct Nd<sup>3+</sup> excitation cross-section for the Nd-doped silica laser glass which was calculated using the same method, and found to be  $1.3 \times 10^{-20}$  cm<sup>2</sup> at 476 nm (a typical cross-section for Nd in glass [79]). The Nd excitation cross-sections estimated for the 476 nm pump laser were  $\sim 10^{-15}$  cm<sup>2</sup> (Table 6.1), five orders of magnitude larger than Nd in the laser glass, and approximately an order of magnitude larger than Er excitation cross-sections reported for Er-doped amorphous nanocluster ( $\sim 10^{-16}$  cm<sup>2</sup> with 476 nm pump wavelength [33]). This implied a more efficient energy transfer from the amorphous nanoclusters to the Nd ions that could be due in part to the large number of closely spaced energy levels above the Nd  $^4F_{3/2}$  level that allows for a wider range of excited nanoclusters to be coupled to the Nd ions compared to Er.

## 6.8 Model

As simplified model of the Si nanocluster and Nd interaction model has been developed formally in an accepted publication. Simple rate equations were used from the model and the effective nanocluster-to-Nd transfer time was estimated to give a measure of the interaction strength. The model is discussed in the manuscript is also discussed here.

It has been established that the amorphous Si nanocluster PL is characteristic of band tail emission in the nanostructures [33, 3]. The nanocluster was therefore approximated as an effective three level system (Fig. 6.2) in which A is the ground

state, B is a distribution of band-tail states, and C is a state above the mobility gap. A carrier is initially excited above the mobility gap, with excitation rate  $R$ , by absorbing a photon. The nanocluster quickly decays to level B when a carrier is trapped in a band-tail state with a rate,  $w_{CB}$ , greater than  $10^9 \text{ s}^{-1}$  [80]. Carrier trapping into a band tail state corresponds to sub-nanosecond timescales (compared to the microsecond time scales of the other rates in the model) therefore  $w_{CB}$  was approximated as infinite. It has been shown that carriers can be transferred from both crystalline and amorphous silicon nanoclusters to Er  $4f$  levels [26, 27, 33], therefore from the band tail state the carrier may decay radiatively, non-radiatively, or transfer the energy to a nearby Nd ion with rates  $w_{BR}$ ,  $w_{BANR}$ , or  $w_{B2}$  respectively (Fig. 6.2).

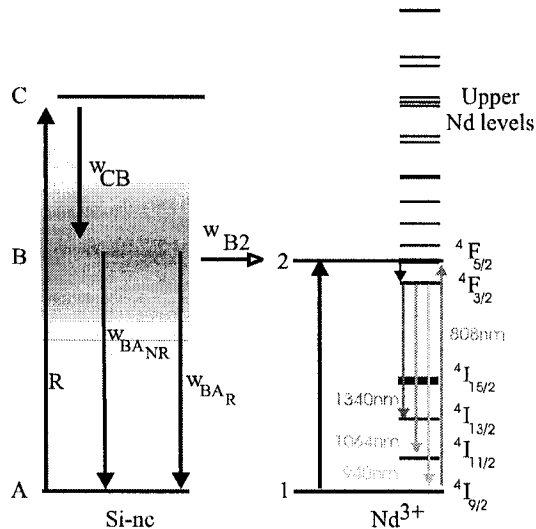


Figure 6.2: Model of amorphous Si nanocluster to Nd ion energy transfer.

The Nd<sup>3+</sup> levels above the  ${}^4F_{3/2}$  level are closely spaced, therefore carriers will rapidly decay via phonons from the upper levels to the  ${}^4F_{3/2}$  level. The rate  $w_{B2}$  therefore represented transfers to all possible Nd levels. Based on the Nd PL intensity (Chapter 5.5) the  ${}^4F_{3/2} \rightarrow {}^4I_{9/2}$  transition was dominant, therefore transitions to the  ${}^4I_{11/2}$  and  ${}^4I_{13/2}$  levels were ignored. Non-radiative Nd decay processes were assumed to be negligible, which is approximately valid as long as Auger transitions from the  ${}^4F_{3/2}$  level are negligible in the low concentration samples (Section 6.5, and in agreement with Er [23] and Nd doped nanocrystals



[62]). Therefore only the radiative decay of the  ${}^4F_{3/2}$  level was considered, and the rate is denoted  $w_{21}$ .

In the low excitation regime the number of nanoclusters and ions in the ground state is approximately constant, and for a pump signal starting at  $t=0$  the population time dependence of the bandtail,  $N_B(t)$ , can be written as

$$\frac{dN_B(t)}{dt} = RN_A - (w_{BA_{NR}} + w_{BA_R} + w_{B2})N_B(t), \quad (6.5)$$

where  $N_A$  is population of unexcited clusters,  $N_B(t)$  is the population of clusters with carriers in the band tails, and  $R$  is the excitation rate. The excitation rate was kept as low as possible (Section 5.6), but high enough to produce a usable signal ( $R \sim 2000$  Hz). Integrating Eq. 6.5 gives an expression for the rise time,

$$N_B(t) = \frac{RN_A}{w_{BA_{NR}} + w_{BA_R} + w_{B2}} * (1 - e^{-(w_{BA_{NR}} + w_{BA_R} + w_{B2})t}). \quad (6.6)$$

Similarly, the time dependence of the  ${}^4F_{3/2}$  level can be written as

$$\frac{dN_2(t)}{dt} = w_{B2}N_B(t) - w_{21}N_2(t), \quad (6.7)$$

where  $N_2(t)$  is the population of the  ${}^4F_{3/2}$  level. Inserting Eq. 6.6 into Eq. 6.7 and solving for  $N_2(t)$  results in Eq. 6.8

$$N_2(t) = \frac{N_A w_{B2} R}{w_{21}(w_{BA_{NR}} + w_{BA_r} + w_{B2})} * \left( 1 - w_{21} \frac{e^{-(w_{BA_{NR}} + w_{BA_r} + w_{B2})t}}{w_{21} - (w_{BA_{NR}} + w_{BA_r} + w_{B2})} \right). \quad (6.8)$$

The radiative rate,  $w_{BA_R}$ , was observed to be approximately  $1 \times 10^6$  s $^{-1}$ , independent of temperature within the resolution of the experiment from 77 to 295 K (in agreement with [81]), and the non-radiative rate,  $w_{BA_{NR}}$ , was obtained from the radiative transition probability,

$$w_{BA_{NR}} = \frac{w_{BA_R}}{I_{Si}(T)} - w_{BA_R}. \quad (6.9)$$

The amorphous silicon nanocluster temperature dependent PL intensity,  $I_{Si}(T)$ ,

has been demonstrated [56, 55, 82] to be fit by the functional form

$$I_{Si}(T) = \frac{A}{1 + Be^{T/T_O}}, \quad (6.10)$$

where  $A$  and  $B$  are fitting parameters, and  $T_O$  is the characteristic temperature proportional to the Urbach energy  $E_U$  (see Section 2.4).  $A$ ,  $B$ , and  $T_O$  were obtained by fitting Eq. 6.10 to the normalized  $I_{Si}$  temperature dependent data, which was normalized by assuming a zero non-radiative rate ( $w_{BANR}=0$ ) and maximum nanocluster PL intensity ( $I_{Si}=1$ ) at  $T = 0$ .

The Nd PL intensity with CW excitation can be written as  $I_{Nd} = bw_{21}N_2(t)$ , where  $b$  is the constant of proportionality and  $t \rightarrow \infty$ . Using Eq. 6.8 at  $t = \infty$  the temperature-dependent Nd intensity under CW excitation can be written as

$$I_{Nd}(T) = \frac{qw_{B2}}{w_{BAR} \frac{1+Be^{T/T_O}}{A} + w_{B2}}, \quad (6.11)$$

The fitting parameters are  $q = bRN_A$  and  $w_{B2}$ , where  $q$  normalized the intensity and  $w_{B2}$  determined the shape of the  $I_{Nd}(T)$  curve. Fitting Eq. 6.11 to the data gave a transfer rate  $w_{b2} = 7.1 \times 10^6 \text{ s}^{-1}$  (Fig. 6.3), which corresponded to a characteristic nanocluster-to-Nd transfer time of approximately  $0.15 \mu\text{s}$ . This rate agreed with suggested transfer times for Er-doped silicon *nanocrystal* composites, which were slightly less than  $1 \mu\text{s}$  [28, 48]. The transfer time was shorter than the nanocluster PL rate ( $w_{BAR} \sim 10^6 \text{ s}^{-1}$ ), consistent with the nanocluster preference to transfer excitation to the Nd ions rather than for carriers to recombine on the clusters. The transfer time depends on the non-radiative decay of the nanoclusters, which was estimated using  $I_{Si}(T)$ , and therefore depends on how  $I_{Si}(T)$  was calculated.

The non-radiative rate  $w_{BANR}$  increased with increasing temperature (Eq. 6.9): according to the model the estimated  $w_{BANR}$  was lower than  $w_{B2}$  at low temperatures, but comparable to it at higher temperatures. This explained the weak temperature dependence observed in the Nd intensity. The Nd PL lifetime, however, did *not* depend on temperature because after the transfer  $w_{BANR}$  had no influence. Furthermore,  $w_{B2}$  was much faster than  $w_{21}$ , therefore the assumption of a two level system used in the Nd cross-section estimate was approximately

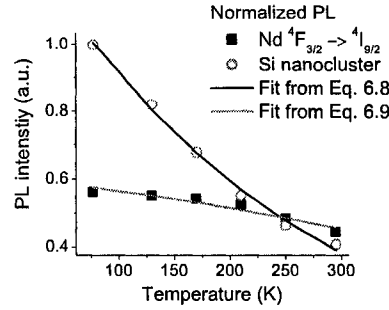


Figure 6.3: Nd and amorphous Si nanocluster PL as a function of temperatures, along with a fit to the Nd PL data from Eq. 6.11 and the fit to the Si PL data from equation 6.10.

valid.

Several assumptions made in the model could lead to errors in the transfer time calculation, some of which could be evaluated. These included constant populations of the ground states, the experimentally determined value of  $w_{BAR}$ , transition to a single Nd level, negligible non-radiative processes from  $Nd^{3+}$ , and the absence of the stretching parameter,  $\beta$ . The steady-state populations of  $N_A$  and  $N_1$  were assumed constant in the model. Fellow grad student A. Hryciw numerically recalculated the population of the  $N_2(t)$  population with  $N_A(t)$  and  $N_1(t)$ , and found the difference in the  $N_2(t)$  population to be less than 1%. The nanocluster radiative decay rate was assumed to be the nanocluster PL rate at low temperature ( $w_{BAR} = 10^6 \text{ s}^{-1}$ ) which was somewhat difficult to accurately determine (see Section 5.2) and therefore could be a source of error. The rate used, however, was consistent with the data and previous work [70]. Two assumptions were made about the dynamics of the Nd excitation: that only a single Nd level was excited by the transfer from the nanocluster, and that state decayed radiatively. Six Nd levels overlap the nanocluster PL band, which can then decay non-radiatively to the  $4F_{9/2}$  level. Since the dynamics of the individual transfers to the Nd levels cannot be resolved, the calculated transfer time can only represent the effective transfer time for the population of the  $4F_{3/2}$  level. The Nd non-radiative processes from that level were assumed to be negligible, as suggested by the pump flux characteristics of the data, however the weak lifetime dependance of  $\tau_{Nd}$  suggested at least one

additional non-radiative process from the  ${}^4F_{3/2}$  was affecting the PL. Finally, the effect of the stretching parameter,  $\beta$ , has been ignored. To my knowledge no publication to date has incorporated  $\beta$  into the silicon nanocluster-RE rate equation modelling.

Despite the simplification of the model and the errors introduced by the assumptions, a good fit was obtained to the  $I_{Si}(T)$  and  $I_{Nd}(T)$  data, and the estimated transfer time agreed with previous estimates for Er in Si *nanocrystal* composites. The transfer rate ( $w_{B2} = 7.1$  MHz) was faster than the measured PL rate, which implied that population inversion may be achieved in Nd at low temperatures by rapidly pumping the nanoclusters. Though  $w_{B2}$  was fast in relation to all other rates in the system, it was several orders of magnitude slower than the excitation rate for Er in bulk Si [83], or Nd in direct bandgap semiconductors [61]. Therefore the transfer process only *appeared* to be efficient because all other rates in the system are comparable or slower.

## Chapter 7

### Conclusion

Amorphous silicon clusters have been shown to sensitize the luminescent transitions in  $\text{Nd}^{3+}$ . The neodymium  $^4F_{3/2}$  level was pumped via a strong non-resonant transfer mechanism from amorphous silicon nanoclusters, and all of the principal  $\text{Nd}^{3+}$  emission bands were observed for specimens annealed at temperatures as low as  $300^\circ\text{C}$ . The low processing temperature (compatible with CMOS fabrication), and the use of an  $\text{SiO}_2$  host make this material compatible with integrated optoelectronic applications. The Nd PL decay lifetime was well described by a stretched exponential with a lifetime of 10 to 30  $\mu\text{s}$ , and  $\beta \sim 0.7$  (Fig. 5.11), where  $\beta$  less than 1 indicated excitation diffusion among the Nd ions or a distribution of lifetimes. Concentration quenching was a significant factor in the Nd PL dynamics at Nd concentrations above 0.3 atomic %, causing the PL intensity to decrease and the decay rate to increase as a result of non-radiative processes. Excited state lifetimes of several hundred  $\mu\text{s}$  are required for population inversion of Nd in traditional laser glasses, therefore to achieve effective population inversion in this medium the excited state lifetime should be increased. This may be achieved with the introduction of network modifiers such as Al or P, and their effects should be explored in future studies. Only a weak temperature dependence of the Nd PL intensity was observed, indicating back-transfer effects were minimal. The dominating non-radiative effect was, therefore, primarily a result of concentration quenching.

The Nd excitation cross-section was calculated to be  $\sim 10^{-15} \text{ cm}^2$  (pump wavelength = 476 nm) by assuming a two-level system at low pump flux. This cross-

section is four orders of magnitude greater than that of Nd in insulating hosts, therefore Nd in the amorphous nanocluster host requires a lower pump flux to achieve high PL intensities. A simple rate equation model of the nanoclusters and Nd ions was developed from which an effective transfer time of  $\sim 0.15 \mu\text{s}$  was estimated. This result is comparable to estimates for the more widely studied energy transfer from silicon *nanocrystals* to  $\text{Er}^{3+}$  ions. The transfer rate ( $\sim 7 \times 10^6 \text{ s}^{-1}$ ) was two orders of magnitude faster than the room temperature Nd PL decay rate for a specimen doped with 0.4 atomic % Nd, implying that population inversion of the  ${}^4F_{3/2}$  level might be achievable in this material. The estimated transfer time, though fast compared to other rates in the system, was several orders of magnitude longer than for the case of Er in bulk Si [84] or Nd in bulk GaAs or GaP [61].

The specimens made in this study feature low processing temperatures, non-resonant optical pumping of the  $\text{Nd}^{3+}$  ions via the nanoclusters, relatively weak back-transfer effects, and an increased effective Nd excitation cross-section compared to Nd-doped silica. These features, along with the relatively fast excitation transfer from the nanoclusters to Nd, make this material promising for further studies. Future investigations may include co-doping with Al or P in an attempt to minimize the deleterious effects of Nd clustering. If the radiative lifetime can be extended by these glass network modifiers, the possibility of population inversion in waveguide or microcavity geometries may be explored. On a fundamental level, future work should incorporate  $\beta$  into the rate equation modelling to give a better description of the nanocluster-RE interactions. This thesis has therefore laid the basic groundwork for future investigations involving non-resonant sensitization of Nd using amorphous Si nanoclusters.

## Bibliography

- [1] J. G. Edwards, *Journal of Physics D-Applied Physics* **1**, 449 (1968).
- [2] <http://www.Wikipedia.com>, Wikipedia fiber optics.
- [3] A. Meldrum, A. Hryciw, A. MacDonald, C. Blois, K. Marsh, J. Wang, and Q. Li, *Journal of Vacuum Science and Technology A* **24**, 713 (2006).
- [4] D. Biggemann and L. R. Tessler, *Materials Science and Engineering B-Solid State Materials for Advanced Technology* **105**, 188 (2003).
- [5] R. M'ghaieth, J. C. Vial, M. Haouari, and H. Maaref, *Journal of Luminescence* **80**, 387 (1998).
- [6] J. C. Pivin, A. Podhorodecki, R. Kudrawiec, and J. Misiewicz, *Optical Materials* **27**, 1467 (2005).
- [7] B. J. Ainslie, S. P. Craig, S. T. Davey, D. J. Barber, J. R. Taylor, and A. S. L. Gomes, *Journal of Materials Science Letters* **6**, 1361 (1987).
- [8] M. Taniguchi, H. Nakagome, and K. Takahei, *Applied Physics Letters* **58**, 2930 (1991).
- [9] G. N. vandenHoven, E. Snoeks, A. Polman, C. vanDam, J. W. M. vanUffelen, and M. K. Smit, *Journal of Applied Physics* **79**, 1258 (1996).
- [10] J. Swiderski, A. Zajac, M. Skorczakowski, Z. Jankiewicz, and P. Konieczny, *Opto-Electronics Review* **12**, 169 (2004).
- [11] G. N. Vandenhoven, J. H. Shin, A. Polman, S. Lombardo, and S. U. Campisano, *Journal of Applied Physics* **78**, 2642 (1995).

- [12] N. Daldosso, D. Navarro-Urrios, M. Melchiorri, L. Pavesi, F. Gourbilleau, M. Carrada, R. Rizk, C. Garcia, P. Pellegrino, B. Garrido, and L. Cognolato, *Applied Physics Letters* **86** (2005).
- [13] A. Polman, G. N. Vandenhoven, J. S. Custer, J. H. Shin, R. Serna, and P. F. A. Alkemade, *Journal of Applied Physics* **77**, 1256 (1995).
- [14] C. Ghisler, W. Luthy, and H. P. Weber, *Optics and Laser Technology* **25**, 25 (1993).
- [15] W. T. Silfvast, *Laser Fundamentals*, 1 ed. (Cambridge University Press, 1996).
- [16] W. J. Miniscalco, Optical and electronic properties of rare earths in glass, in *Rare earth doped fiber lasers and amplifiers*, edited by Digonnet, , 2 ed., 1987.
- [17] S. Poole, D. Payne, and M. Fermann, *Journal of Lightwave technology* **LT-4** (1986).
- [18] C. G. Atkins, J. F. Massicott, J. R. Armitage, R. Wyatt, B. J. Ainslie, and S. P. Craigryan, *Electronics Letters* **25**, 910 (1989).
- [19] Laming, *Electronic Letters* **25**, 12 (1989).
- [20] E. Snoeks, G. N. Vandenhoven, A. Polman, B. Hendriksen, M. B. J. Diemeer, and F. Priolo, *Journal of the Optical Society of America B-Optical Physics* **12**, 1468 (1995).
- [21] K. Arai, H. Namikawa, K. Kumata, T. Honda, Y. Ishii, and T. Handa, *Journal of Applied Physics* **59**, 3430 (1986).
- [22] X. W. Zhao, S. Komuro, H. Isshiki, S. Maruyama, Y. Aoyagi, and T. Sugano, *Applied Surface Science* **114**, 121 (1997).
- [23] J. H. Shin, M. J. Kim, S. Y. Seo, and C. Lee, *Applied Physics Letters* **72**, 1092 (1998).
- [24] G. Franzo, V. Vinciguerra, and F. Priolo, *Applied Physics A* **69**, 3 (1999).



- [25] J. Heitmann, M. Schmidt, M. Zacharias, V. Y. Timoshenko, M. G. Lisachenko, and P. K. Kashkarov, *Materials Science and Engineering B-Solid State Materials for Advanced Technology* **105**, 214 (2003).
- [26] I. N. Yassievich and A. S. Moskalenko, *Materials Science and Engineering B-Solid State Materials for Advanced Technology* **105**, 192 (2003).
- [27] K. Watanabe, M. Fujii, and S. Hayashi, *Journal of Applied Physics* **90**, 4761 (2001).
- [28] D. Pacifici, G. Franzo, F. Priolo, F. Iacona, and L. Dal Negro, *Physical Review B* **67** (2003).
- [29] F. Priolo, G. Franzo, D. Pacifici, V. Vinciguerra, F. Iacona, and A. Irrera, *Journal of Applied Physics* **89**, 264 (2001).
- [30] F. Priolo, G. Franzo, F. Iacona, D. Pacifici, and V. Vinciguerra, *Materials Science and Engineering B-Solid State Materials for Advanced Technology* **81**, 9 (2001).
- [31] A. Hryciw, J. Laforge, C. Blois, M. Glover, and A. Meldrum, *Advanced Materials* **17**, 845 (2005).
- [32] H. Lee, J. H. Shin, and N. Park, *Optics Express* **13**, 9881 (2005).
- [33] A. Hryciw, C. Blois, A. Meldrum, T. Clement, R. DeCorby, and Q. Li, *Optical Materials* , 873 (2006).
- [34] N. I. Nweke, R. J. Runser, S. R. McNown, and J. B. Khurgin, *Optical Engineering* **44** (2005).
- [35] P. Maguire, L. Barry, T. Krug, w. Guo, J. ODowd, M. Lynch, A. Bradley, J. Donegan, and H. Folliot, *Journal of lightwave technology* **24**, 2683 (2006).
- [36] J. A. Caird, A. J. Ramponi, and P. R. Staver, *Journal of the Optical Society of America B-Optical Physics* **8**, 1391 (1991).
- [37] Y. C. Ratnakaram, M. A. Altaf, R. P. S. Chakradhar, J. L. Rao, and J. Ramakrishna, *Physica status solidi (b)* **236**, 200 (2003).

- [38] A. Kenyon, *Semiconductor Science and Technology* **20**.
- [39] J. I. Pankove, *Optical processes in semiconductors*, 1 ed. (Dover Publications Inc., 180 Varick Street, New York, N.Y. 10014, 1975).
- [40] G. Davies, *Physics Reports-Review Section of Physics Letters* **176**, 83 (1989).
- [41] O. B. Gusev, M. S. Bresler, P. E. Pak, I. N. Yassievich, M. Forcales, N. Q. Vinh, and T. Gregorkiewicz, *Physical Review B* **64**, 075302 (2001).
- [42] A. Prokofiev, *Physical Review - B* **82**, 045214 (2005).
- [43] R. M. Almeida, A. C. Marques, and R. Cabeca, *Journal of Sol-Gel Science and Technology* **31**, 317 (2004).
- [44] E. Snoeks, P. G. Kik, and A. Polman, *Optical Materials* **5**, 159 (1996).
- [45] S. V. Gaponenko, *Optical Properties of Semiconductor Nanocrystals* Cambridge Studies in Modern Optics, 1 ed. (University of Cambridge, Cambridge, United Kingdom).
- [46] M. Fujii, K. Imakita, K. Watanabe, and S. Hayashi, *Journal of Applied Physics* **95**, 272 (2004).
- [47] L. X. Yi, J. Heitmann, R. Scholz, and M. Zacharias, *Journal of Physics-Condensed Matter* **15**, S2887 (2003).
- [48] P. G. Kik and A. Polman, *Journal of Applied Physics* **88**, 1992 (2000).
- [49] M. Dovrat, Y. Goshen, J. Jedrzejewski, I. Balberg, and A. Sa'ar, *Physical Review B* **69** (2004).
- [50] P. G. Kik, M. J. A. deDood, K. Kikoin, and A. Polman, *Applied Physics Letters* **70**, 1721 (1997).
- [51] E. Gross, D. Kovalev, N. Kunzner, J. Diener, F. Koch, V. Y. Timoshenko, and M. Fujii, *Physical Review B* **68** (2003).
- [52] M. J. Estes and G. Moddel, *Physical Review B* **54**, 14633 (1996).

- [53] N. F. Mott, *Philosophical Magazine B-Physics of Condensed Matter Statistical Mechanics Electronic Optical and Magnetic Properties* **43**, 941 (1981).
- [54] A. Hryciw, A. Meldrum, K. S. Buchanan, and C. W. White, *Nuclear Instruments and Methods in Physics Research Section B-Beam Interactions with Materials and Atoms* **222**, 469 (2004).
- [55] Y. Kanemitsu, *Journal of Luminescence* **100**, 209 (2002).
- [56] R. W. Collins, M. A. Paesler, and W. Paul, *Solid State Communications* **34**, 833 (1980).
- [57] S. Roberts and G. Parker, *Optical materials* **6**, 99 (1996).
- [58] J. Ha, C. Bae, and S. Nam, *APL* **82**, 3436 (2003).
- [59] Q. Wang, N. K. Dutta, and R. Ahrens, *Journal of Applied Physics* **95**, 4025 (2004).
- [60] P. Kik, *Energy transfer in erbium doped optical waveguides based on silicon*, PhD thesis, University of Utrecht FOM-Institute for Atomic and Molecular Physics, 2002.
- [61] A. Taguchi and K. Takahei, *Journal of Applied Physics* **79**, 4330 (1996).
- [62] S. Y. Seo, M. J. Kim, and J. H. Shin, *Applied Physics Letters* **83**, 2778 (2003).
- [63] M. J. Weber, *Physical Review B* **4**, 2932 (1971).
- [64] K. Arai, H. Namikawa, K. Kumata, Y. Ishii, H. Tanaka, and I. Iida, *Japanese journal of Applied Physics* **22**, L397 (1983).
- [65] D. Mullin, Personal communication, 2004.
- [66] A. Meldrum, K. S. Buchanan, A. Hryciw, and W. White, *Advanced Materials* **16**, 31 (2004).
- [67] J. Wang, X. F. Wang, Q. Li, A. Hryciw, and A. Meldrum, *Philosophical Magazine* ((in press)).

- [68] Y. Kanemitsu, Y. Fukunishi, and T. Kushida, *Applied Physics Letters* **77**, 211 (2000).
- [69] C. G. Van de Walle, *Physical Review B* **53**.
- [70] T. Muschik and R. Schwartz, *Journal of Non-Crystalline Solids* **619**, 164 (1993).
- [71] M. Langlet, C. Coutier, W. Meffre, M. Audier, J. Fick, R. Rimet, and B. Jacquier, *Journal of Luminescence* **96**, 295 (2002).
- [72] J. Dong, M. Bass, and C. Walters, *Journal of the Optical Society of America, B* **21**, 454 (2004).
- [73] A. L. Cook and H. D. Hendricks, *Applied Optics* **37**, 3276 (1998).
- [74] J. Kakalios, R. A. Street, and W. B. Jackson, *Physical Review Letters* **59**, 1037 (1987).
- [75] R. Chen, *Journal of Luminescence* **102**.
- [76] L. Pavesi and C. Matteo, *Physical Review B* **48**.
- [77] J. Linnros, N. Lalic, A. Galeckas, and V. Grivickas, *Journal of Applied Physics* **86**, 6128 (1999).
- [78] B. Sturman, E. Podivilov, and M. Gorkunov, *Physical Review Letters* **91**.
- [79] J. Furthner and A. Penzkofer, *Optical and Quantum Electronics* **24**, 591 (1992).
- [80] W. B. Jackson, C. Doland, and C. C. Tsai, *Physical Review B* **34**, 3023 (1986).
- [81] K. Wang, D. X. Han, M. Kemp, and M. Silver, *Applied Physics Letters* **62**, 157 (1993).
- [82] R. B. Wehrspohn, J. N. Chazalviel, F. Ozanam, and I. Solomon, *European Physical Journal B* **8**, 179 (1999).

- [83] A. Matsuoka and S. Tohno, JAP **84**, 4471 (2000).
- [84] A. Taguchi, K. Takahei, M. Matsouka, and T. S, Journal of Applied Physics **84**.
- [85] B. GmbH and Hickl, *PMS-300, PMS-400 and PMS-400A 800Mz Gated Photon Counters/Multiscalers Manual* (Becker and Hickl, Berlin, Germany, 2004).

## Appendix A

### Exciton energy levels

Electron-hole pairs interacting only via the Coulomb potential form a hydrogen-like bound state known as an exciton. This imaginary particle can be described by the same Hamiltonian as the hydrogen atom, and similarly by its Bohr radius and Rydberg energy. These can be calculated for an electron-hole pair in a medium by replacing the mass of the proton and the electron with the effective masses of the hole and electron in the medium,  $m_h^*$  and  $m_e^*$ :

$$a_B^* = \frac{\epsilon}{\epsilon_0} \frac{\mu}{\mu^*} a_B \quad (\text{A.1})$$

and

$$Ry = \frac{1}{4\pi} \frac{e^2}{2\epsilon a_b^*} = \frac{\mu e^4}{2\epsilon^2 \hbar^2}, \quad (\text{A.2})$$

where  $\mu^{-1}$  is the inverse of the reduced mass,  $m_e^{*-1} + m_h^{*-1}$ , and  $\epsilon$  is the permittivity of Si. In Si the Bohr radius,  $a_B$ , is estimated to be 4.3 nm, and the Rydberg energy (ground state of the model),  $Ry^*$ , to be 15 meV [45].

## Appendix B

### Quantum confinement

The density of states of a system confined in one or more dimensions can be described as

$$\rho(E) \propto E^{d/2-1}, \quad (\text{B.1})$$

where  $d$  is the dimensionality of the system ( $d = 1, 2, 3$ ), and energy,  $E$ , is measured for electrons from the bottom of the conduction band. Discrete sub-bands due to quantum confinement appear as in the “particle in a box” problem; the density of states obeys Eq. B.1 within the sub-bands (constant for  $d=2$ ,  $\propto 1/\sqrt{E}$  for  $d=1$ ). In the case of  $d=0$  there is a finite number of atoms in the system, and finite numbers of elementary excitations. The energy levels in the quantum dot may be described as a particle in a cubic (or spherical) potential,

$$E_{n_x, n_y, n_z} = \frac{\hbar^2 \pi^2}{2\mu L^2} (n_x^2 + n_y^2 + n_z^2), \quad (\text{B.2})$$

where  $L$  is the length of the box side,  $\mu$  is the effective mass of the electron and hole in the nanocluster, and  $n$  is 1, 2, 3, (...). This effective mass approximation assumes the effective mass in the nanocluster is identical to that in the bulk crystal. Here the density of states is a set of discrete delta-like functions whose energy difference increases as the particle size decreases.

In the weak confinement regime the energy of the electron hole pair is

$$E_{n=1,m=1,l=0} = E_g - R_y^* + \frac{\pi^2 \hbar^2}{2(m_e^* + m_h^*)a^2} = E_g - 0.5 \frac{e^2}{\epsilon} \frac{1}{a_b} + \frac{1}{(m_e^* + m_h^*)} \frac{\pi^2 \hbar^2}{2a^2}, \quad (\text{B.3})$$

where  $R_y^*$ ,  $m_e^*$ , and  $m_h^*$  are the Rydberg energy and electron/hole masses in the nanocluster,  $a$  is the radius of the nanocluster,  $\epsilon$  is the permittivity in the nanocluster, and  $a_b$  is the Bohr radius of the electron-hole pair in the nanocluster.

In the strong confinement regime the energy of the pair is

$$E_{n=1,m=1,l=0} = E_g - 1.786 \frac{e^2}{\epsilon} \frac{1}{a} + \frac{a}{\mu} \frac{\pi^2 \hbar^2}{2a^2}. \quad (\text{B.4})$$



## Appendix C

### Acousto-optic modulator

The modulator consists of a piezoelectric speaker transmitting radio-frequency sound waves through a piece of glass. The compression and expansion plane waves change the glass density, resulting in a periodically varying index of refraction. Light Brillouin scatters off the index pattern, Bragg diffracting into a number of resolvable spots, where

$$\sin\theta = \frac{m\lambda}{2\Lambda}, \quad (\text{C.1})$$

and  $\theta$  is the angle of scattered light from zeroth order mode,  $m$  is the mode order (an integer),  $\lambda$  is the wavelength of modulated light, and  $\Lambda$  is the wavelength of modulating sound. The intensity of light diffracted depends on the sound intensity, the zeroth mode can typically be modulated from 15% to 99% of its intensity, and the first mode from 0% to 88%.

## Appendix D

### Photomultiplier tube

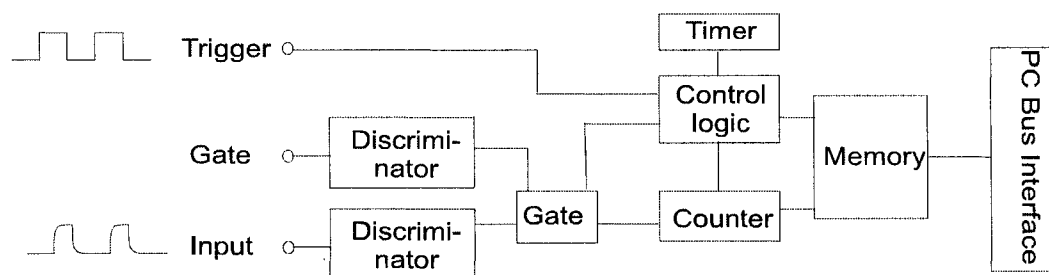


Figure D.1: photon counter block diagram. The discriminator selects the minimum signal voltage of one count, counted after the trigger voltage is applied.

The PMT sends the photon counter input a pulse, passed through a voltage discriminator to select the minimum voltage that qualifies as a count. The resolution of the scan depends on the gate pulse sent to the gate discriminator. If the leading edge of the signal discriminator output occurs within the gate pulse an output pulse is sent to the counter. The maximum resolution was 250 ns.

The PMTs cooling, gain, and on/off switch were controlled by the detector control card on the desktop computer, and the photon counter triggered off the modulator. A pre-amplifier was used in conjunction with the PMT. Most PMTs have 20-50 mV pulses at maximum gain [85]; though still within the photon counter detection range the pre-amplifier protects the detector by avoiding the use of a high current required for low voltages. The use of the pre-amplifier also improves the signal to noise ratio and increases threshold accuracy. The trigger threshold of

the photon counter was set to 0.136V, approximately 1/2 the signal generators voltage, and triggered on the rise. The channel rates were monitored to find the initial signal incident on the PMT, integrating over 25  $\mu\text{sec}$  (repeated every 0.2 seconds). Once a signal was found and amplified accordingly, the lifetime data were collected in the multi-scalar mode over up to 1 million time sweeps with a minimum time step of 0.25  $\mu\text{sec}$ . In this setting the counter results for sequential time steps are stored; resulting in a pulse density vs. time (wave form) plot.